Monthly Notices
of the
ROYAL ASTRONOMICAL SOCIETY

Mon. Not. R. Astron. Soc. **424,** 1672–1693 (2012) doi:10.1111/j.1365-2966.2012.21131.x

Line transfer through clumpy, large-scale outflows: Lyα absorption and haloes around star-forming galaxies

Mark Dijkstra[1]★ and Roban Kramer[2]

[1]*Max-Planck-Institut fuer Astrophysik, Karl-Schwarzschild-Str. 1, 85741 Garching, Germany*
[2]*Institute for Astronomy, ETH Zurich, Wolfgang-Pauli-Strasse 27, CH-8093 Zurich, Switzerland*

Accepted 2012 April 18. Received 2012 April 18; in original form 2012 March 14

ABSTRACT

We present constrained radiative transfer calculations of Lyα photons propagating through clumpy, dusty, large-scale outflows, and explore whether we can quantitatively explain the Lyα haloes that have been observed around Lyman break galaxies. We construct phenomenological models of large-scale outflows which consist of cold clumps that are in pressure equilibrium with a constant-velocity hot wind. First, we consider models in which the cold clumps are distributed symmetrically around the galaxy and in which the clumps undergo a continuous acceleration in its 'circumgalactic' medium (CGM). We constrain the properties of the cold clumps (radius, velocity, H I column density and number density) by matching the observed Lyα absorption strength of the CGM in the spectra of background galaxies. We then insert a Lyα source in the centre of this clumpy outflow, which consists of 10^5–10^6 clumps, and compute observable properties of the scattered Lyα photons. In these models, the scattered radiation forms haloes that are significantly more concentrated than observed. In order to simultaneously reproduce the observed Lyα absorption line strengths and the Lyα haloes, we require – preferably bipolar – outflows in which the clumps decelerate after their initial acceleration. This deceleration is predicted naturally in 'momentum-driven' wind models of clumpy outflows. In models that simultaneously fit the absorption and emission-line data, the predicted linear polarization is $\sim$30–40 per cent at a surface brightness contour of $S = 10^{-18}$ erg s^{-1} cm^{-2} arcsec^{-2}. Our work illustrates clearly that Lyα emission-line haloes around star-forming galaxies provide valuable constraints on the cold gas distribution and kinematics in their CGM, and that these constraints complement those obtained from absorption-line studies alone.

Key words: radiative transfer – scattering – ISM: jets and outflows – galaxies: formation – intergalactic medium – quasars: absorption lines.

1 INTRODUCTION

Deep narrow-band imaging has revealed that star-forming galaxies are surrounded by large ($R \sim 100$ kpc) Lyα haloes (Hayashino et al. 2004; Steidel et al. 2011; Matsuda et al. 2012; see also Fynbo, Møller & Warren 1999; Rauch et al. 2008). The origin of these haloes is still disputed, but they likely encode valuable information on both the distribution and kinematics of cold gas around galaxies. Understanding this so-called 'circumgalactic' medium (CGM) is vital to our understanding of galaxy formation and evolution.

Zheng et al. (2011b) attribute the presence of extended Lyα haloes to resonant scattering of Lyα photons in the CGM. In this model, the gravitational potential well of the dark matter halo that is hosting the galaxy gives rise to inflows of overdense, ionized, circumgalactic gas. This infalling, overdense gas contains residual H I that is opaque to Lyα radiation (also see Barkana & Loeb 2003; Santos 2004; Dijkstra, Lidz & Wyithe 2007; Iliev et al. 2008; Laursen, Sommer-Larsen & Razoumov 2011), and can scatter a significant fraction of the Lyα flux that escapes from galaxies into diffuse haloes.

However, observations of the gas in the CGM of Lyman break galaxies (LBGs) indicate that the 'cold' (i.e. $T \sim 10^4$–10^5 K) gas is almost exclusively outflowing: low-ionization metal absorption lines are typically blueshifted relative to the galaxies' systematic redshift, and the covering factor of these blueshifted absorption lines are large (Steidel et al. 2010). Steidel et al. (2010) argue that these outflows – which are not present in the simulations by Zheng et al. (2011b) – play an important role in the Lyα transport problem, and scattering through outflows can explain (i) in particular

★E-mail: dijkstra@mpa-garching.mpg.de

the extended red wing of the Lyα spectral shape of the Lyα line that is observed in their galaxies and (ii) the observed Lyα haloes around their galaxies (Steidel et al. 2011). Steidel et al. (2010) provide a simple model for the Lyα scattering process in which a spherically symmetric distribution of outflowing clumps surrounds each galaxy. The 'covering factor' of clumps on the sky decreases, and their outflow velocity increases with distance from the galaxy.

Steidel et al. (2010) treat the scattering of Lyα photons in only an approximate way, and it is not clear whether a full radiative transfer calculation would yield similar results. Given the simple geometry of the clumpy outflow model that Steidel et al. (2010) propose, it is straightforward to treat the scattering process itself more accurately and to investigate whether their model can indeed quantitatively reproduce the observed Lyα haloes. It is important to test the scattering model and to investigate if other processes need to be invoked to explain the presence of extended Lyα haloes around (all) star-forming galaxies. These other processes include, for example, resonant scattering in the ionized inflowing CGM (Zheng et al. 2011b) and spatially extended Lyα *emission* (as opposed to scattering) from supernova-driven outflows (Mori, Umemura & Ferrara 2004) or from the cold gas streams that provide galaxies with their gas in cosmological hydrodynamical simulations (e.g. Fardal et al. 2001; Furlanetto et al. 2005; Dijkstra & Loeb 2009; Faucher-Giguère et al. 2010; Goerdt et al. 2010; Rosdahl & Blaizot 2012). Indeed, recent work has indicated that the so-called 'cold flows' may reproduce the observed Lyα absorption line strengths in the CGM of simulated LBGs quite well (Fumagalli et al. 2011), which raises the question as to whether the Lyα haloes are also related to cold streams.[1]

The goal of this paper is simple: to test whether scattering through a large-scale clumpy, possibly dusty, outflow can give rise to spatially extended Lyα haloes around star-forming galaxies and, importantly, whether such models are consistent with the observed Lyα absorption strength of the CGM as measured in the spectra of background galaxies (as in Steidel et al. 2010). In order to properly model the scattering process, we modify the Monte Carlo radiative transfer code for Lyα propagation from Dijkstra, Haiman & Spaans (2006), so that it works on arbitrary distributions of dusty clumps.

Having such a code is very useful, as understanding Lyα transfer through (clumpy, dusty) outflows is relevant in a wider range of astrophysical contexts. First, Lyα radiative transfer through outflows affects the imprint that reionization leaves on the visibility of the Lyα emission line from high-redshift galaxies (Santos 2004; Dijkstra & Wyithe 2010; Dijkstra, Mesinger & Wyithe 2011; Dayal & Ferrara 2012). Secondly, scattering through outflows strongly affects the large-scale clustering of Lyα-selected galaxies in the post-reionization epoch (Wyithe & Dijkstra 2011; Zheng et al. 2011a), which is directly relevant for, for example, the HETDEX[2] dark energy experiment (Hill et al. 2004). Finally, Lyα line transfer through clumpy, dusty (not necessarily outflowing) media is of interest because it can strongly boost the fraction of Lyα photons that can escape from the interstellar medium (ISM) of a galaxy, possibly even enhancing the equivalent width (EW) of the line as it emerges from the galaxy (Neufeld 1991; Haiman & Spaans 1999; Hansen & Oh 2006; Finkelstein et al. 2009, but see also Scarlata et al. 2009; Kornei et al. 2010).

This paper is organized as follows. In Section 2 we introduce the basic quantities that describe a general clump distribution. In Section 3 we describe our model for the cold clumps embedded within a hot, large-scale outflow, and how we constrain the parameters of this model by matching to the absorption-line data of Steidel et al. (2010). This procedure fixes the properties of the scattering medium. We describe how we perform Lyα radiative transfer calculations through this medium in Section 4. We present the main results of our calculations and explore how these depend on our assumed initial line profile and dust content of the clumps in Section 5. In Section 6.1 we explore more realistic velocity profiles of the cold clumps. We discuss model uncertainties and broader implications of our work in Section 7 before presenting our main conclusions in Section 8.

In this paper we express frequency ν in terms of the dimensionless variable $x \equiv (\nu - \nu_\alpha)/\Delta\nu_\alpha$. Here, $\nu_\alpha = 2.46 \times 10^{15}$ Hz denotes the frequency corresponding the Lyα resonance (similarly $\lambda_\alpha = 1215.67$ Å corresponds to wavelength of this transition) and $\Delta\nu_\alpha \equiv \nu_\alpha\sqrt{2kT/m_{\rm p}c^2} \equiv \nu_\alpha v_{\rm th}/c$. Here, T denotes the temperature of the gas that is scattering the Lyα radiation. Table 1 gives an overview of symbols used in this paper. The cosmological parameters used throughout our discussion are $(\Omega_{\rm m}, \Omega_\Lambda, h) = (0.3, 0.7, 0.7)$, which is consistent with Komatsu et al. (2009).

2 SOME GENERAL CLUMP STATISTICS

We denote the number density of clumps at a separation r from the source (located at $r = 0$) by $n_{\rm c}(r)$ and their outflow velocity by $v_{\rm c}(r)$. We denote the radius of a clump by $R_{\rm c}(r)$. The number density of neutral hydrogen atoms inside clumps is denoted by $n_{\rm H\,I}(r)$. The *average* H I-column density of the cold clumps is denoted by $N_{\rm H\,I}(r)$ and is given[3] by $N_{\rm H\,I}(r) \equiv 4n_{\rm H\,I}(r)R_{\rm c}(r)/3$. Finally, the *covering factor* $f_{\rm c}(r)$ is given by $f_{\rm c}(r) = n_{\rm c}(r)\sigma_{\rm c}(r)$, where $\sigma_{\rm c}(r) = \pi R_{\rm c}(r)^2$ denotes the geometric cross-section of a clump of radius $R_{\rm c}(r)$. The covering factor $f_{\rm c}(r)$ thus has units of length^{-1} and plays a role that is analogous to opacity $\kappa(r)$ in a homogeneous medium. We caution the reader that our definition of covering factor differs from that adopted by Hansen & Oh (2006), who defined the covering factor to be the mean *total* number of clumps encountered along a random line of sight (which we denote by $\mathcal{N}_{\rm clump}$, see below) and which is therefore analogous to optical depth in a homogeneous medium. Table 1 summarizes the symbols that we use to describe the clump properties.

Many useful properties of the clumps can be expressed in terms of this covering factor.

[1] 'Gravitational heating' of cold flow gas in dark matter haloes of mass $M_{\rm halo} \sim 10^{12}\,{\rm M}_\odot$, the approximate mass of the dark matter halo masses associated with LBGs (e.g. Rudie et al. 2012, and references therein), can give rise to Lyα luminosities of the order of $L \lesssim 10^{42}\,{\rm erg\,s^{-1}}$ (Haiman, Spaans & Quataert 2000; Dijkstra & Loeb 2009; Faucher-Giguère et al. 2010; Goerdt et al. 2010), which is an order of magnitude fainter than the observed luminosities of Lyα haloes around LBGs. This rules out the possibility that gravitationally heated cold flows contributed significantly to the observed luminosity of Lyα haloes (but see Rosdahl & Blaizot 2012). However, it is possible to increase the Lyα emissivity of cold stream gas if sources embedded in the stream photoionize the gas in the streams (e.g. Dijkstra & Loeb 2009; Latif et al. 2011).

[2] http://hetdex.org/

[3] The average column density is given by $N_{\rm H\,I}(r) = \frac{1}{\pi R_{\rm c}^2(r)}\int_0^{R_{\rm c}(r)} {\rm d}y\; 2\pi y \hat{N}_{\rm H\,I}(y)$, where $\hat{N}_{\rm H\,I}(y)$ denotes the total H I column density at impact parameter y through the clump, and is given by $\hat{N}_{\rm H\,I}(y) = 2\sqrt{R_{\rm c}^2 - y^2}n_{\rm H\,I}$. We can evaluate the integral analytically and obtain $N_{\rm H\,I}(r) = 4n_{\rm H\,I}(r)R_{\rm c}(r)/3$.

Table 1. Summary of symbols used throughout this paper.

	Symbols describing clump properties
r	Physical separation of a clump from the source (kpc)
b	'Impact' parameter (kpc)
$n_{\rm c}$	Number density of clumps (in kpc^{-3})
$n_{\rm H}$	Number density of H-nuclei (i.e. protons, in cm^{-3})
$n_{\rm H\,I}$	Number density of neutral hydrogen atoms (in cm^{-3})
$R_{\rm c}$	Radius of the clump
$\sigma_{\rm c}$	Cross-sectional area of the clump (in kpc^2): $\sigma_{\rm c} = \pi R_{\rm c}^2$
$m_{\rm c}$	Clump mass (in M$_\odot$)
$N_{\rm H\,I}$	Column density of H I through the clump, weighted by cross-sectional area (in cm^{-2}): $N_{\rm H\,I} = 4R_{\rm c}n_{\rm H\,I}/3$
$f_{\rm c}$	Covering factor (in kpc^{-1}): $f_{\rm c} = n_{\rm c}\sigma_{\rm c}$
$T_{\rm c}$	Gas temperature in the cold clumps
$v_{\rm th}$	'Thermal' velocity of H I in cold clumps (km s^{-1}): $v_{\rm th} = \sqrt{2kT_{\rm c}/m_{\rm p}}$
	Symbols used for Lyα radiative transfer
ν_α	Lyα resonance frequency: $\nu_\alpha = 2.46 \times 10^{15}$ Hz
$\Delta\nu_\alpha$	Thermal line broadening (Hz): $\Delta\nu_\alpha \equiv \nu_\alpha v_{\rm th}/c$
x	Dimensionless photon frequency: $x \equiv (\nu - \nu_\alpha)/\Delta\nu_\alpha$
σ_0	Lyα absorption cross-section at line centre: $\sigma_0 = 5.88 \times 10^{-14}(T_{\rm c}/10^4\,{\rm K})^{-1/2}\,{\rm cm}^2$
$\sigma_\alpha(x)$	Lyα absorption cross-section at frequency x (cm^2): $\sigma_\alpha(x) = \sigma_0\phi(x)$
$\phi(x)$	Voigt function at frequency x We adopt the normalization such that $\phi(x=0) = 1$, and therefore that $\int \phi(x)\,{\rm d}x = \sqrt{\pi}$.
$a_{\rm v}$	Voigt parameter: $a_{\rm v} = 4.7 \times 10^{-4}(T_{\rm c}/10^4\,{\rm K})^{-1/2}$
$\boldsymbol{k}_{\rm in/out}$	Unit vector that denotes the propagation direction of the photons before/after scattering
$\boldsymbol{e}_{\rm in/out}$	Unit vector that denotes the electric vector of the photons before/after scattering
μ	Cosine of the scattering angle: $\mu = \boldsymbol{k}_{\rm in}\cdot\boldsymbol{k}_{\rm out}$
$P(\mu)$	Scattering phase function We adopt the normalization $\int_{-1}^{1}{\rm d}\mu\ P(\mu) = 4\pi$.

(i) The 'mean free path' between clumps $\lambda_{\rm c}(r) = 1/[n_{\rm c}(r)\sigma_{\rm c}(r)] = 1/f_{\rm c}(r)$.

(ii) Hence, the mean number of clumps along a random sightline through the distribution of clumps is

$$\mathcal{N}_{\rm clump}(b) = 2\int_b^{r_{\rm max}} \frac{r\,{\rm d}r}{\sqrt{r^2-b^2}}\,f_{\rm c}(r), \qquad (1)$$

where b denotes the 'impact parameter' of the sightline, which is the perpendicular distance of the sightline to the origin $r = 0$. We integrate out to radius $r_{\rm max} = 250$ kpc, which corresponds to the radius where the observed absorption vanishes (this corresponds to $R_{\rm eff}$ in Steidel et al. 2010).

(iii) The 'shell covering factor' $F_{\rm c}(r)$ which denotes the fraction of the area of a spherical shell at radius r that is embedded within clumps [denoted by $C_f(r)$ by Martin & Bouché 2009] is given by

$$\begin{aligned} F_{\rm c}(r) &= \int_0^\infty {\rm d}r'\ n_{\rm c}(r')\sigma_{\rm c}(r|r') \\ &\approx \pi\int_{r-R_{\rm c}(r)}^{r+R_{\rm c}(r)} {\rm d}r'\ n_{\rm c}(r')\Big[R_{\rm c}^2(r') - (r-r')^2\Big] \\ &\approx \frac{4}{3}n_{\rm c}(r)\pi R_{\rm c}^3(r) = \frac{4}{3}f_{\rm c}(r)R_{\rm c}(r) = f_{\rm v}(r), \end{aligned} \qquad (2)$$

where $\sigma_{\rm c}(r|r')$ denotes the area of the clump whose centre lies at radius r' on the sphere of radius r. The approximation on the second line is only true when ${\rm d}R_{\rm c}(r)/{\rm d}r \ll 1$, which is generally true in this paper. The quantity $f_{\rm v}(r)$ denotes the volume filling factor of clumps at radius r, and is given by $f_{\rm v}(r) = n_{\rm c}(r)\frac{4}{3}\pi R_{\rm c}^3(r)$.

If the total mass outflow rate is given by $\dot{M}_{\rm out}$, then the total mass flux through each radial shell is given by $\dot{M}_{\rm out}/4\pi r^2$. The mass density[4] in clumps at radius r is then $\rho_{\rm c}(r) = \dot{M}_{\rm out}/4\pi r^2 v_{\rm c}(r)$. If the clumps have a constant mass, then the number density of clumps is $n_{\rm c}(r) = \dot{N}_{\rm c}/4\pi r^2 v_{\rm c}(r)$, where $\dot{N}_{\rm c}$ is the total rate at which clumps are ejected. For a constant $\dot{N}_{\rm c}$, the radial dependence of $\sigma_{\rm c}(r) = f_{\rm c}(r)/n_{\rm c}(r) \propto r^2 f_{\rm c}(r)v_{\rm c}(r)$, i.e. $R_{\rm c}(r) \propto r f_{\rm c}^{1/2}(r)v_{\rm c}^{1/2}(r)$. The total number of clumps is given by $N_{\rm clump} = \int_0^{r_{\rm max}}{\rm d}r\ 4\pi r^2 n_{\rm c}(r)$.

3 MODELLING CLUMPY OUTFLOWS AROUND LBGs

The theory of large-scale outflows around star-forming galaxies is extremely complex. Furthermore, the kinematics and distribution of cold gas in the outflow is particularly uncertain. Energy and momentum deposition by radiation, supernova explosions and cosmic rays create hot overpressurized bubbles, which sweep up the surrounding ISM into dense, cold shells of gas (see e.g. the introduction of Dalla Vecchia & Schaye 2008; Ceverino & Klypin 2009, and references therein). These 'supershells' accelerate as they break out of ISM into the lower density CGM, making them subject to hydrodynamical (Rayleigh–Taylor) instabilities. The overall acceleration – and hence the velocity that the cold gas can reach – depends sensitively on when the cold gaseous shells fragment: after fragmentation, the hot gas can expand freely through the fragmented shell, which reduces the outward pressure on the cold gas (e.g. Cooper et al. 2008; Fujita et al. 2009, and references therein).

Fujita et al. (2009) have shown that a spatial resolution of $\sim$0.1 pc is required to resolve the hydrodynamical instabilities, and highlight the physics that likely affects the detailed properties of the cold gas in the outflow. For example, magnetic fields may prevent fragmentation of the gas shells and thus allow the cold gas to reach larger velocities; thermal conduction may further stabilize the cold shells. On the other hand, photoionization may heat the cold clumps to higher temperatures, which reduces the density contrast with the hot wind, which may in turn enhance the fragmentation of the cold shells.

Regardless of these complex model details, we expect cold fragments of gas to be entrained within a hot wind, and that these cold clumps have outflow velocities that are less than or equal to the hot wind outflow velocity. The fate of these cold clumps is unclear:

[4] The analogy with radiation is illuminating: suppose a central source of radiation (instead of mass) has a luminosity L. Then the energy flux through radial shell r is $s = L/4\pi r^2$. The energy density in the radiation field is $u = L/4c\pi r^2$ (e.g. Rybicki & Lightman 1979; also see fig. 1 of Dijkstra & Loeb 2008b).

Klein, McKee & Colella (1994) showed that the cold clumps are destroyed on a short time-scale as a result of hydrodynamical instabilities at the cold cloud–hot wind interface. Recent studies have shown that including thermal conduction and magnetic fields in the calculations may significantly enhance the survival probability of the cold clumps (see Cooper et al. 2008; Fujita et al. 2009, and references therein). Additionally, new cold clumps might form from thermal instabilities in the hot wind (or hot halo gas; see e.g. Joung, Bryan & Putman 2012). These two effects (cloud destruction and formation) introduce further uncertainties to the spatial distribution of cold clumps.

The previous illustrates clearly that ab initio modelling of cold gas in a large-scale galactic outflow is extremely complex. We therefore adopt a simple phenomenological model for the cold clouds in the outflow as in Martin & Bouché (2009). Following Steidel et al. (2010), we assume that these clouds are distributed symmetrically around the galaxy. This simple model contains parameters, which we will constrain by matching the absorption-line data of Steidel et al. (2010).

3.1 The model

The total mass outflow rate is given by $\dot{M}_{\rm out} \equiv \eta \times$ SFR, where 'η' denotes the 'mass loading' factor and SFR the star formation rate (e.g. Oppenheimer & Davé 2006; Davé, Finlator & Oppenheimer 2012). We assume SFR $= 34\,{\rm M}_\odot\,{\rm yr}^{-1}$ which corresponds to the median ultraviolet (UV) based dust-corrected SFR of all 92 continuum-selected galaxies that were used to create the stacked Lyα image that revealed the Lyα halo surrounding them.[5] We assume the outflow consists of a 'cold' component which is embedded in a 'hot' component, both of which are in pressure equilibrium. The total cold (hot) mass outflow rate is denoted by $\dot{M}_{\rm c}$ ($\dot{M}_{\rm h}$). We further assume that the clumps all have the same mass (and radius) when they are driven out, and that their mass does not change while they propagate out. Under this assumption the mass of an individual clump, $m_{\rm c}$, relates to the total number of clumps in our Monte Carlo simulation as

$$m_{\rm c} = \frac{\dot{M}_{\rm c}}{N_{\rm clump}} \int_0^{r_{\rm max}} \frac{{\rm d}r}{v_{\rm c}(r)} \equiv \frac{\eta_{\rm c}{\rm SFR}}{N_{\rm clump}} \int_0^{r_{\rm max}} \frac{{\rm d}r}{v_{\rm c}(r)}, \quad (3)$$

where we introduced the cold-gas mass loading factor $\eta_{\rm c} \equiv \dot{M}_{\rm c}/{\rm SFR}$. For a given $N_{\rm clump}$ we need to know the velocity profile $v_{\rm c}(r)$ to compute the mass in the cold clumps. In order to compute the H I gas density inside the clump, we need to know pressure in the hot wind.

Following Martin & Bouché (2009) we assume a steady-state constant velocity hot wind, for which mass conservation implies $\rho_{\rm h}(r) = \dot{M}_{\rm h}/(4\pi r^2 v_{\rm h})$, in which $v_{\rm h}$ denotes the outflow velocity of the hot wind. The number density of particles in the hot wind is $n_{\rm h}(r) \approx \rho_{\rm h}(r)/m_{\rm p}$, where we assumed that the mean molecular weight $\mu_{\rm h} \approx 1$. Both components obey $p(r)n^{-\gamma}(r) = {\rm constant}$, where γ denotes the gas' adiabatic index, and their gas pressure is given by $p(r) = n(r)k_{\rm B}T(r)$. Assuming pressure equilibrium between the hot and cold gas, we find

$$T_{\rm h}(r) = T_{\rm h,0}\left(\frac{r}{r_{\rm min}}\right)^{2-2\gamma_{\rm h}},$$
$$T_{\rm c}(r) = T_{\rm c,0}\left(\frac{r}{r_{\rm min}}\right)^{-2\gamma_{\rm h}+2\gamma_{\rm h}/\gamma_{\rm c}},$$
$$n_{\rm c,H} = \frac{T_{\rm h,0}}{T_{\rm c,0}} \frac{\dot{M}_{\rm h}}{m_{\rm p}\,4\pi r_{\rm min}^2 v_{\rm h}} \left(\frac{r}{r_{\rm min}}\right)^{-2\gamma_{\rm h}/\gamma_{\rm c}}. \quad (4)$$

Here, $\gamma_{\rm c}$ [$\gamma_{\rm h}$] denotes the adiabatic index of the cold (hot) gas, and $T_{\rm c,0}$ ($T_{\rm h,0}$) denotes the temperature of the cold (hot) gas at some reference radius $r_{\rm min}$, which denotes the 'launch' or 'break out' radius (as in Steidel et al. 2010). We further assume that the (constant) velocity of the hot wind is related to the temperature of the hot gas at the break out radius as $v_{\rm h} \approx 940(T_{\rm h,0}/10^7\,{\rm K})^{0.5}\,{\rm km\,s^{-1}}$ (Martin & Bouché 2009). If we substitute some 'typical' values, then we find

$$n_{\rm c,H} \approx 36\left(\frac{T_{\rm h,7}^{1/2}\dot{M}_{\rm h,10}}{T_{\rm c,4} r_{\rm min,1}^2}\right)\left(\frac{r}{r_{\rm min}}\right)^{-2\gamma_{\rm h}/\gamma_{\rm c}} {\rm cm}^{-3}, \quad (5)$$

where $T_{\rm h,7} \equiv T_{\rm h,0}/10^7\,{\rm K}$, $T_{\rm c,4} \equiv T_{\rm c,0}/10^4\,{\rm K}$, $r_{\rm min,1} = r_{\rm min}/{\rm kpc}$ and $\dot{M}_{\rm h,10} \equiv \dot{M}_{\rm h}/(10\,{\rm M}_\odot\,{\rm yr}^{-1})$. The number density $n_{\rm c,H}$ refers to the total number density of hydrogen nuclei in the clump. When the clump self-shields, we expect all of the hydrogen to be neutral. Recent hydrodynamical simulations of cosmological volumes indicate that a decent approximation to the full radiative transfer of ionizing radiation is obtained by assuming that gas self-shields when the number density exceeds some threshold value of $n_{\rm crit} \gtrsim 6 \times 10^{-3}\,{\rm cm}^{-3}$ (e.g. Nagamine, Choi & Yajima 2010). In our model, we will assume that the number density of neutral hydrogen atoms $n_{\rm H\,I,c}(r) = n_{\rm c,H}$ for $n_{\rm c,H} \geq n_{\rm crit}$. When $n_{\rm c,H} < n_{\rm crit}$, we assume photoionization equilibrium with the UV background, and that the neutral fraction of hydrogen by number is given by $x_{\rm H\,I} = \alpha_{\rm B} n_{\rm c,H}/\Gamma_{\rm bg}$. Here, $\alpha_{\rm B} = 2.6 \times 10^{-13}(T_{\rm c}/10^4)^{-0.7}\,{\rm cm^3\,s^{-1}}$ denotes the case B recombination coefficient and $\Gamma_{\rm bg} = 5 \times 10^{-13}\,{\rm s^{-1}}$ denotes the photoionization rate (Faucher-Giguère et al. 2008).

To complete the description of our outflow model, we need to assume $v_{\rm c}(r)$. As discussed previously, this velocity profile is not well known and depends sensitively on when the cold gas shells fragment and on whether cold clouds form from the hot wind as a result of thermal instabilities. We follow the empirical approach of Steidel et al. (2010), who assumed that the *acceleration* of the cold clumps scales as $a_{\rm c}(r) = Ar^{-\alpha}$, which results in a velocity profile of the form

$$v_{\rm c}(r) = \left(\frac{2A}{\alpha - 1}\right)^{0.5} \left(r_{\rm min}^{1-\alpha} - r^{1-\alpha}\right)^{0.5}, \quad (6)$$

for $\alpha > 1$ (Steidel et al. 2010), where A is a constant that sets the velocity at $r \to \infty$, v_∞, i.e. $v_\infty = \sqrt{2Ar_{\rm min}^{1-\alpha}/(\alpha-1)}$. We do not consider models with $\alpha \leq 1$ in this paper (see below).[6]

Formally, our model has thus 10 parameters, which include $r_{\rm min}$, α, v_∞, $T_{\rm h,0}$, $T_{\rm c,0}$, $\gamma_{\rm h}$, $\gamma_{\rm c}$, $\eta_{\rm c}$, $\eta_{\rm h}$ and $N_{\rm clump}$. For most of these parameters we have decent constraints, and they are not free. For example, Steidel et al. (2010) inferred from their observations that $1.15 < \alpha < 1.95$, $v_\infty = 800\,{\rm km\,s^{-1}}$ and adopted $r_{\rm min} = 1\,{\rm kpc}$, which

[5] The galaxies that were used to compile the stacked Lyα image are not the same galaxies for which the CGM was probed with background galaxies (see Section 7.1). However, both sets of galaxies were selected in a very similar way and have very similar physical properties. For example, the median SFR of the 'CGM galaxies' was SFR $= 30\,{\rm M}_\odot\,{\rm yr}^{-1}$ (Erb et al. 2006), which is practically indistinguishable from the value that we have adopted.

[6] In the simulations of Dalla Vecchia & Schaye (2008), the wind velocity increases with r simply because the gas at a given radius has a velocity that is close to the minimum velocity it must have had to reach that radius in the finite time since the launch of the wind. Having $v_{\rm c}(r)$ increase with r therefore does not solely represent models in which the clumps accelerate with radius.

Table 2. Outflow model parameters that we adopt in our models.

Model	$r_{\rm min}$ (kpc)	α	v_∞ (km s^{-1})	$T_{\rm h,7}$	$T_{\rm c,4}$	$\eta_{\rm h}$	$\eta_{\rm c}$	$N_{\rm clump}$	$\gamma_{\rm c}$	$\gamma_{\rm h}$	$m_{\rm c}$ (M$_\odot$)
Models in which $a_{\rm c}(r) = Ar^{-\alpha}$ (Section 3.1)											
Model I	1.0	1.4	780	1.0	0.3	0.6	0.7	10^6	1.0	1.0	8×10^3
Model II	1.0	1.5	790	1.0	0.5	0.9	1.1	10^5	1.0	1.0	1.2×10^5
Model III	1.2	1.4	834	0.9	0.7	3.6	0.9	10^5	1.0	1.2	9×10^4
Models in which $a_{\rm c}(r) = Ar^{-\alpha} - GM(r)/r^2$ (Section 6.1).											
Models IV–V	1.0	1.4	N/A	1.0	0.9	0.2	0.9	8.5×10^5	1.0	1.0	1×10^4

is close to theoretical estimates of the blow out radius (Martin & Bouché 2009). The observationally inferred hot wind temperatures lie in the range $T_{\rm h} = 10^6$–10^7 K for dwarf galaxies (Martin 1999), but could be larger by a factor of $\sim$10 in starburst galaxies (e.g. Strickland & Heckman 2009). Cold gas at temperatures $T_{\rm c} > 10^4$ K would efficiently cool down to $T_{\rm c} \sim 10^4$ K, below which gas cooling becomes less efficient. Further cooling is possible because of metals, but it is unclear to which temperatures the gas can cool in the cold clumps and to what extent the clumps are heated as a result of their interaction with the hot wind (and/or as a result of photoheating). We will consider values of $\log T_{\rm c} = 2$–4. Oppenheimer & Davé (2006) could reproduce the observed amount of C IV absorption in quasar spectra at $z = 2$–5 with large-scale (momentum-driven) outflows arising from star-forming galaxies, for a *total* mass loading factor $\eta \equiv \eta_{\rm c} + \eta_{\rm h} = \sigma_0/\sigma$. Here, σ denotes the velocity dispersion of the galaxy and $\sigma_0 = 150\,{\rm km\,s^{-1}}$ (Oppenheimer & Davé 2008). The observed dispersion of the Hα line in the galaxies that were used to construct the stacked Lyα image is $\sigma_{\rm H\alpha} \sim 100$–$150\,{\rm km\,s^{-1}}$ (see fig. 4 of Steidel et al. 2010). Under the reasonable assumption that $\sigma_{\rm H\alpha}$ provides a good measure of σ, we require that the total mass loading factor is close to unity. However, we caution that direct observational constraints on η are uncertain by a factor of at least a few (Genel et al. 2012, and references therein). The adiabatic index of the cold gas is $1 \leq \gamma \leq 5/3$, where $\gamma = 1$ [$\gamma = 5/3$] corresponds to isothermal (adiabatic) gas.

In this paper, we only consider isothermal cold clouds, i.e. $\gamma_{\rm c} = 1$, because we found that for models with $\gamma_{\rm c} > 1.2$ generally the cold clumps are compressed too much, which gives rise to EW–b curves that decline too steeply with b. We also only consider models with either $\gamma_{\rm h} = 1$ or 1.2. As we will show, in models with $\gamma_{\rm h} = 1.2$ the cold clumps expand more rapidly, which causes $n_{\rm c,H} < n_{\rm crit}$, and the H I column density of the cold clumps declines too fast for significant scattering of Lyα photons. Finally, we only consider $N_{\rm clump} = 10^6$ and 10^5. This choice for $N_{\rm clump}$ translates into clump masses in the range $m_{\rm c} = 10^4$–10^5 M$_\odot$ (see Table 2). We stress that our main results are insensitive to the adopted value for $N_{\rm clump}$.

3.2 Constraining the free parameters of the model with absorption-line data

As was discussed above, each outflow model contains 10 parameters, seven of which are allowed to vary within a reasonably well-known range. Each model is therefore parametrized by the 7D parameter vector $\boldsymbol{P} \equiv (r_{\rm min}, \alpha, v_\infty, T_{\rm h,0}, T_{\rm c,0}, \eta_{\rm c}, \eta_{\rm h})$. For each $\boldsymbol{P}$ we obtain a distribution of cold clumps that contain neutral atomic hydrogen. Steidel et al. (2010) have measured the average Lyα absorption line strength at impact parameter b from galaxies by analysing the spectra of background galaxies. We can use these observations to constrain the components of $\boldsymbol{P}$.

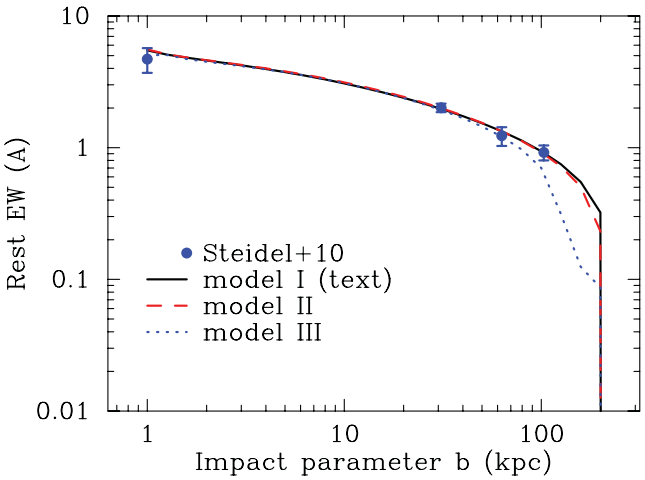

Figure 1. This figure shows the mean absorption line strength – quantified by the rest-frame EW – in the Lyα line as a function of impact parameter b. Blue filled circles indicate the observations by Steidel et al. (2010). The three lines indicate EW as a function of b for the three models (models I–III) for the large-scale outflow (see text for details on the model). These models are used as input to our Lyα radiative transfer calculations.

Specifically, Steidel et al. (2010) have measured mean absorption EW (rest frame) in the Lyα line at four impact parameters. These measurements are shown as filled blue circles in Fig. 1. The EW (at impact parameter b) is defined as

$$\mathrm{EW}(b) = \lambda_\alpha \frac{\Delta v_\alpha}{v_\alpha} \int_{-\infty}^{+\infty} {\rm d}x \{1 - \exp[-\tau(x, b)]\}. \quad (7)$$

The integral is over the dimensionless frequency x (see Table 1), and $\exp[-\tau(x, b)]$ denotes the fraction of the flux at frequency x that is transmitted to the observer.

Evaluating this transmission is more complicated for a clumpy medium than for a homogeneous medium. For example, in the hypothetical case of $\mathcal{N}_{\rm clump}(b) = 0.1$ we expect only 10 per cent of all sight-lines with impact parameter b to pass through a clump, and the outflow is transparent for the remaining 90 per cent of the sight-lines. The absorption line strength is then $\mathrm{EW}(b) = \mathrm{EW}_{\rm clump}(r)/10$, where $\mathrm{EW}_{\rm clump}(r)$ denotes the EW as a result of absorption by a single clump. In the more general case, the transmission $\exp[-\tau(x, b)]$ is a product of the transmission by individual segments along the sightline, i.e. $\exp[-\tau(x, b)] = \prod_{i=1}^{N_{\rm s}} \exp[-\tau(x, b, s_i)]$. Here, $\exp[-\tau(x, b, s_i)]$ denotes the fraction of the flux that is transmitted by clumps in line segment 'i', which lies at line-of-sight coordinate s_i, which has length Δs_i, and which lies at a distance $r_i \equiv \sqrt{b^2 + s_i^2}$ from the galaxy. This transmission $\exp[-\tau(x, b, s_i)] = p_{{\rm clump},i} \exp[-\tau_{\rm clump}(x')] + 1 - p_{{\rm clump},i}$. Here, $p_{\rm clump}$ denotes the probability that a clump lies on line segment 'i' and $\exp[-\tau_{\rm clump}(x')]$ denotes the total fraction of the flux that is transmitted by the clump.

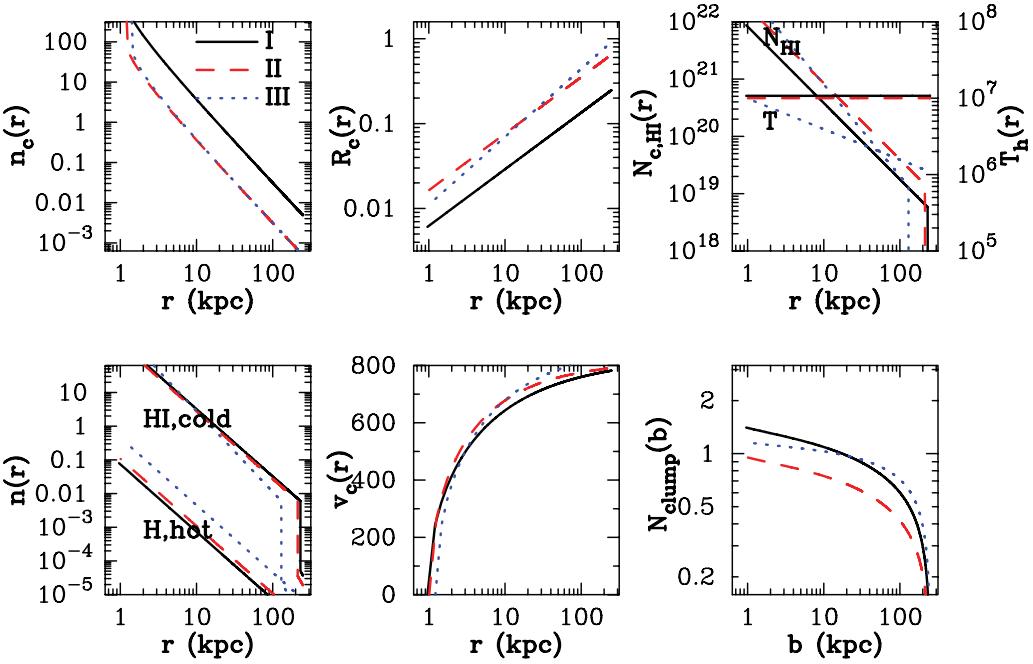

Figure 2. The plots give a more detailed look at models I–III of the cold clumps in the large-scale outflow. We show the number density of clumps $n_c(r)$ in proper kpc^{-3} in the upper-left panel. The upper central panel shows the clump radius in proper kpc as a function of r. The upper-right panel shows the H I column density (in cm^{-2}) through an individual clump located at radius r. The lower-right panel shows the number density of H I atoms in the clump (in cm^{-3}), while the lower central panel shows the velocity profile (in km s^{-1}). Finally, the lower-right panel shows the number of clumps a random sightline with impact parameter b intersects.

Note that because of the outflow velocity of the clump, x' is related to x via a Doppler boost (see below). The probability that line segment 'i' contains a clump is given by[7] $p_{\rm clump,\,\it i} = f_{\rm c}(r)\Delta s_i$, and we obtain

$$\exp[-\tau(x,b)] = \prod_{i=1}^{N_{\rm s}} \left(\Delta s_i\, f_{\rm c}(r_i) \exp[-N_{\rm c,H\,I}(r_i)\sigma_\alpha(x')] + 1 - \Delta s_i\, f_{\rm c}(r_i) \right). \quad (8)$$

Here, line segment 'i' covers the range $[s_{\rm min} + (i-1)\Delta s_i,\, s_{\rm min} + i\Delta s_i]$, where $s_{\rm min} = -\sqrt{r_{\rm max}^2 - b^2}$ and $\Delta s_i = 2|s_{\rm min}|/N_{\rm s}$. Furthermore, $\sigma_\alpha(x')$ denotes the Lyα absorption cross-section evaluated at frequency x' in the frame of the clump, i.e. $x' = x - \frac{v_{\rm c}(r)}{v_{\rm th}} \boldsymbol{e}_{\rm s} \cdot \boldsymbol{e}_{\rm r}$. Here, $\boldsymbol{e}_{\rm s}$ ($\boldsymbol{e}_{\rm r}$) denotes a unit vector along the line of sight towards the galaxy (along the radial vector). We stress that the background galaxies do not provide *sightlines* through the CGM of the foreground galaxy. Because of their finite physical sizes, they instead probe 'sight cylinders' of some radius $r_{\rm cyl}$ through the CGM. However, it is easy to show that equation (8) also applies to cylinders of radius $r_{\rm cyl}$ provided that $r_{\rm cyl} \ll b$, which is the case for the observations at $b \gtrsim 30$ kpc since $r_{\rm cyl}$ is around a few kpc (e.g. Law et al. 2012). Formally, this formalism is not correct at $b \sim 0$. However, we have explicitly verified that a more detailed calculation[8] reduces the predicted EW by only $\lesssim$20 per cent at $b = 0$ for $r_{\rm cyl} \leq 5$ kpc.

To find models that fit the data of Steidel et al. (2010) we use a Markov chain Monte Carlo (MCMC) simulation to probe the parameter space spanned by $\boldsymbol{P}$. Our exploration of the parameter space is rather simple: our goal is to find models that provide a good fit to the data, whether these models are physically plausible in the context of our model and to explore whether these same models can give rise to the observed Lyα haloes. We will not present probability distribution functions for the elements of $\boldsymbol{P}$, and will not explore the correlations that exist between them. Given the simplified nature of the model, this would distract us from the main purpose of our analysis.

From the Markov chains[9] we select three models, which we denote with models I–III. We summarize the parameters of these models in Table 2. Fig. 1 compares the observed EW as a function of b to the predictions by the models. The black solid line, red dashed line and blue dotted line represent model I, model II and model III, respectively. All models clearly provide a good fit to the data.

Fig. 2 shows some properties of the cold clumps for all three models, where we use the same line style and colour representation as in Fig. 1. We discuss the clump properties in more detail below.

[7] Formally, we do not allow the clumps to overlap in our Lyα Monte Carlo calculations, which modifies the probability $p_{\rm clump,\,\it i} = f_{\rm c}(r)\Delta s_i \times p(\text{no clump at } \Delta s \leq 2R_{\rm c}) \sim f_{\rm c}(r)\Delta s_i \times [1 - 4 f_{\rm c}(r) R_{\rm c}(r)]$. We have explicitly checked that this difference makes no difference in practice because of the low volume filling factor for the cold clumps.

[8] In the case of a cylinder, we replace $p_{\rm clump,\,\it i}$ with the fraction of the area of the background galaxy, $A_{\rm bg}$, that is covered by clumps in cylinder segment 'i', which is given by $\frac{2\pi\Delta s_i}{A_{\rm bg}} \int_o^{r_{\rm cyl}} {\rm d}x\; x\; n_{\rm c}(u) A_{\rm c}(u)$, where $u^2 = x^2 + s_i^2$.

[9] We generate 10 chains that contain 2000 steps and simply select the best-fitting model from all 10 chains. For each step we compute the likelihood $\mathcal{L}(\boldsymbol{P}) = \exp(-\chi^2/2) P_{\rm prior}(\boldsymbol{P})$, where $\chi^2 = \sum_{i=1}^{4} ({\rm EW}_{{\rm mod},i} - {\rm EW}_{{\rm obs},i})^2/\sigma_{{\rm EW},i}^2$. We assume flat priors on $T_{\rm c}$, $\eta_{\rm h}$ and $\eta_{\rm c}$, but restrict ourselves to the range $2 < \log T_{\rm c,0} < 4$, $0.1 < \eta_{\rm h} < 10$, $0.1 < \eta_{\rm c} < 10$ (i.e. outside this range, the prior probability is set to zero). We assume Gaussian priors for $r_{\rm min}$ $[(\bar{r}, \sigma) = (1.0, 1.0)]$, α $[(\bar{\alpha}, \sigma) = (1.5, 0.4)]$, v_∞ $[(\bar{v}, \sigma) = (800.0, 100.0)]$ and $\log T_{\rm h,0}$ $[(\bar{T}, \sigma) = (7.0, 0.5)]$, but restrict ourselves to $0 < r_{\rm min} < 3.0$ kpc, $0.5 < \alpha < 2.0$ (Steidel et al. 2010), $500 < v_\infty < 1000$ km s^{-1} and $5.0 < \log T_{\rm h,0} < 8.0$.

(i) Model I: the clump radii increase from $R_c < 0.01$ kpc to $R_c \sim 0.1$ kpc at $r = 100$ kpc. The H I column density of the clumps falls from $N_{c,HI} \sim 2 \times 10^{20}\,cm^{-2}$ at $r = 10$ kpc to $N_{HI} \sim 10^{19}\,cm^{-2}$ at $r = 100$ kpc. The lower-left panel shows that the H I number density stays above n_{crit} all the way out to $r \sim 200$ kpc, and that then the H I number density drops off fast. The central lower panel shows that the outflow velocity of the clumps increases rapidly at small radii and that it barely increases further at $r \gtrsim 10$ kpc (this plot is also shown in fig. 23 of Steidel et al. 2010). Finally, the lower-right panel shows that a random sightline at impact parameter b intersects ∼1 clump out to $b = 100$ kpc, after which it decreases rapidly.

(ii) Model II: most differences between this model and model I are easily understood – the number density of clumps is lower by a factor of 10 as a result of the lower total number of clumps. In order to yield the same absorption line strength, the decrease in $n_c(r)$ is compensated for by an increase of their radii (upper central panel). The H I number density in the cold clumps is set entirely by the properties in the hot gas, and hence remains identical (lower-left panel). As a result of the unchanged H I number density and the enhanced clump radii, the total H I column density is correspondingly larger (upper-right panel). Finally, because of the enhanced H I column density of individual clumps, $\mathcal{N}_{clump}(b)$ must be smaller for model II in order to reproduce the observed EW(b) (lower-right panel).

(iii) Model III: the number density of clumps is almost identical to that of model II, which is because this number density is determined mostly by the total mass outflow rate of cold gas (comparable for both models) as well as the velocity profile (also comparable for both models). The temperature of the hot gas decreases with radius from $T_h \sim 10^7$ to 10^6 K in this model (upper-right panel), pressure equilibrium also implies that the number density of H I atoms decreases faster in the model (lower-left panel). Because we fixed the clump mass, the clump radius is therefore increasing more rapidly with radius in model III than in model II (upper central panel).

3.3 Generating a random realization of clumps

We generate random realizations of models I–III as follows. For each of the N_{clump} clumps in our model, we first generate a random unit vector $\boldsymbol{e}_i$. Then we generate a random radial coordinate r_i of the clump from

$$\mathcal{R} = \int_0^{r_i} dr\; 4\pi r^2 n_c(r), \tag{9}$$

where $\mathcal{R}$ is a random number between 0 and 1. The centre of the clump 'i' is then given by $\boldsymbol{x}_i \equiv r_i \boldsymbol{e}_i$. We then check whether clump 'i' overlaps with any of the previously generated $i - 1$ clumps. In case it does, we generate a new random unit vector $\boldsymbol{e}_i$, until clump 'i' does not overlap with any of the other clumps. We then proceed to generating the position of clump 'i+1'. The velocity, temperature, radius, H I number density and dust content are specified fully for a given r_i and a given model (the dust content will be discussed in Section 5.2).

Once we have random realizations for each model, we shoot random sight-lines at a range of impact parameters (100 sightlines at each impact parameter) and compute the mean Lyα absorption strength as a function of impact parameter. We show the results of this exercise in Fig. 3, where we use the same line colours and style to represent the different models as in the previous plots. Our discrete realizations of clumps also give rise to Lyα absorption at

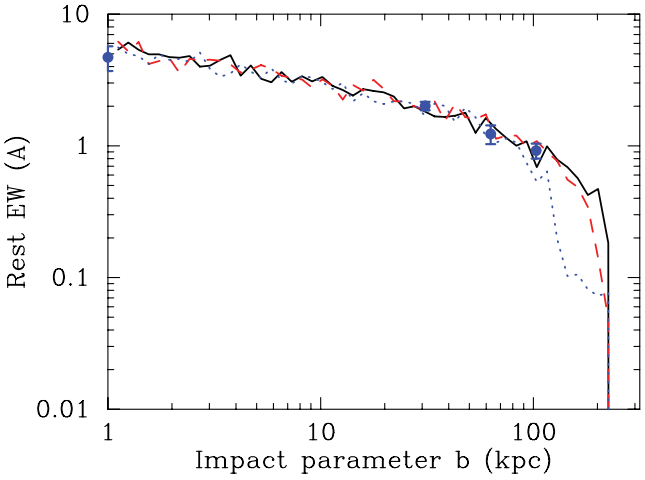

Figure 3. Same as Fig. 1, but for random realizations of models I–III. This figure illustrates that we have generated representative random realizations of our best-fitting models. It also provides an independent check of our predicted EW as a function of b in equation (8).

levels that are in excellent agreement with the data. This provides an independent check of the accuracy of equation (8) and that we have generated representative random realizations of our best-fitting models.

4 THE Lyα TRANSFER MODEL

4.1 Monte Carlo calculations

Our Monte Carlo Lyα radiative transfer code was developed, tested and described in more detail in Dijkstra et al. (2006). For our current work we modify the code in several ways.

(i) We can follow the transfer through an arbitrary distribution of spherical clumps. Each clump is assigned a location, a radius, a hydrogen number density, a dust number density, a temperature and a (radial) velocity. This differs from the applications presented in Dijkstra et al. (2006), where we focused on single spherically symmetric gas clouds. In Dijkstra et al. (2006) the single clump was divided into a large number of spherically concentric shells, to each of which we assigned a velocity, H I density and temperature. In this work, we do not allow for gradients of temperature, etc. across the clump (although our code can be modified for this purpose).

(ii) We include the impact of dust on the radiative transfer process following Laursen, Sommer-Larsen & Andersen (2009). We assume an 'Small Magellanic Cloud (SMC)' type frequency dependence of the dust absorption cross-section. However, this frequency dependence is practically irrelevant over the narrow range of frequencies which are covered by Lyα photons (see Laursen et al. 2009, for details). When Lyα photons scatter off a dust grain, we assume that the scattering is described by a Henyey–Greenstein phase function with asymmetry parameter $g = 0.73$ (Laursen et al. 2009, and references therein). Scattering of UV radiation by SMC-type dust gives rise to little linear polarization (see fig. 5 of Draine 2003), and for simplicity we shall assume that scattering by dust grains does not polarize Lyα radiation. For the work presented in this paper we will assume that the albedo, which denotes the ratio of the scattering to the total cross-section, is $A = 0.0$ (see Section 5.2). We assume that the relation between dust *absorption* opacity $\tau_{D,a}$ and the colour excess $E(B - V)$ is given by $\tau_{D,a} = 10.0E(B - V)$ (see also Verhamme, Schaerer & Maselli 2006).

(iii) Because we want the option to study clumpy outflows that are not spherically symmetric, we generate surface brightness profiles with the so-called 'peeling algorithm' or the 'next event estimator'. This technique has been employed in many previous studies of Lyα transfer (e.g. Zheng & Miralda-Escudé 2002; Cantalupo et al. 2005; Tasitsiomi 2006; Laursen & Sommer-Larsen 2007; Faucher-Giguère et al. 2010; Kollmeier et al. 2010; Barnes et al. 2011). A more detailed description of how we generate images can be found in Appendix A1.2.

(iv) As in Dijkstra & Loeb (2008a) we compute polarization of scattered radiation. Polarization calculations have thus far focused solely on spherically symmetric gas distributions.

We point out that our code allows us to perfectly 'resolve' the Lyα transfer inside of clumps with arbitrarily small radii (in this case $R_c \lesssim 10$ pc) (see Section 3.2) within our large (diameter ∼500 kpc) outflow.

4.2 Analytic calculations

Under the assumption that the Lyα photons scatter only once – which is reasonable as we will argue below – we can compute the surface brightness profile [$S(b)$] as well as the polarization profile [$\mathcal{P}(b)$] analytically as

$$S(b) = S_l(b) + S_r(b) \tag{10}$$

$$\mathcal{P}(b) = \frac{|S_l(b) - S_r(b)|}{S_l(b) + S_r(b)}, \tag{11}$$

where $S_l(b)$ and $S_r(b)$ denote polarized fluxes (Rybicki & Loeb 1999; Dijkstra & Loeb 2008a), which are given by

$$\left.\begin{matrix} S_l(b) \\ S_r(b) \end{matrix}\right\} = \left(\frac{\rm kpc}{\rm asec}\right)^2 \int_{-\infty}^{\infty} {\rm d}x \int_{-\infty}^{\infty} {\rm d}s \; \frac{r}{b} \times \frac{3}{4} \times s_{\rm in}(x, b, s) \times f_c(s, b) \times (1 - \exp[-\tau_{\rm clump}(x', s, b)]) \times f_{\rm esc}(x'', b, s) \times \left\{ \begin{matrix} \mu^2 \\ 1 \end{matrix} \right. , \tag{12}$$

where the term (kpc/asec)^2 converts the surface brightness into units erg s^{-1} cm^{-2} arcsec^{-2}. Furthermore, $s_{\rm in}(x, b, s)$ denotes the total incoming flux at location (b, s) and frequency x, where s denotes the line-of-sight coordinate (see Fig. B1). We can write $s_{\rm in}(x, b, s) = s_0 \frac{n(x)}{4\pi r^2} \exp(-\tau[s, b, x])$, in which s_0 denotes the total observed Lyα flux of the source if no scattering occurred at all,[10] $r \equiv \sqrt{s^2 + b^2}$ and $\exp(-\tau[s, b, x])$ denotes the total fraction of the flux at frequency x that has *not* been scattered out of the line of sight yet. The term $\exp(-\tau[s, b, x])$ is computed as in equation (8). The optical depth $\tau_{\rm clump}(x', s, b) = N_{\rm H\,I,c}(r)\sigma_\alpha(x')$ denotes the optical depth through the clump at radius r at frequency x. In the frame of the clump, photons of frequency x appear at $x' = x - v_c(r)/v_{\rm th}$. The last line contains the scattering phase function, in which $\mu = -s/r$, and accounts for the fact that photons are not scattered in all directions with equal probability. Finally, $f_{\rm esc}(x'', b, s)$ is the probability that photons that are scattered towards the observer are detected. This probability can again be computed as in equation (8), but note that after scattering the photon's frequency has been changed to $x'' = x + (\mu - 1)v_c(r)/v_{\rm th}$. We present a complete derivation of this equation in Appendix B.

[10] The flux s_0 relates to the intrinsic luminosity, L_α, of the source simple as $s_0 \equiv L_\alpha 4\pi d_L^2(z)$, where $d_L(z)$ denotes the luminosity distance to redshift z.

5 RESULTS

In our Monte Carlo calculations we emit $N_\gamma = 10^5$ Lyα photons in the centre of the clumpy outflow for each model, and randomly draw the initial frequency of each emitted photon from a Gaussian with a standard deviation of $\sigma = 150\,{\rm km\,s^{-1}}$. This is close to the typical dispersion of the observed Hα lines in the sample, which is about $\sigma_{\rm H\alpha} \sim 100\,{\rm km\,s^{-1}}$ (see fig. 4 of Steidel et al. 2010). We assume that the luminosity of the central source is $L_\alpha = 3.4 \times 10^{43}\,{\rm erg\,s^{-1}}$. This luminosity corresponds to the intrinsic Lyα luminosity of a galaxy that is forming stars at a rate SFR = 34 M$_\odot$ yr^{-1}, which corresponds to the median UV-based dust-corrected SFR of all 92 continuum-selected galaxies that were used to create the stacked Lyα image. We thus implicitly assume that the escape fraction of Lyα photons from the dusty ISM into the large-scale outflow is[11] $f_{\rm esc} = 100$ per cent. The predicted surface brightness scales linearly with $f_{\rm esc}$. The luminosity $L_\alpha = 3.4 \times 10^{43}\,{\rm erg\,s^{-1}}$ which at $z = 2.65$ translates into $s_0 = 5.9 \times 10^{-16}\,{\rm erg\,s^{-1}\,cm^{-2}}$, which is relevant for our analytic calculations.

Throughout, we represent the observed Lyα surface brightness profile by the function $S(b) = S_0 \exp[-b/b_c]$, where b denotes the impact parameter in kpc. Here, $S_0 = 2.4 \times 10^{-18}\,{\rm erg\,s^{-1}\,cm^{-2}\,arcsec^{-2}}$ and $b_c = 25.2$ kpc. This function provides an accurate fit to the average Lyα observed in the full sample of 92 continuum-selected galaxies with Lyα imaging (Steidel et al. 2011), and is shown as red solid lines in the following figures.

We represent results from our Monte Carlo calculations with black filled solid circles, which contain error bars. We obtain these points by averaging the six surface brightness (and polarization) profiles that we obtain by viewing the clump distribution from six different directions (see Section 4.1). Uncertainties on the these points indicate the standard deviation from this average.

5.1 Dust-free clumpy outflows

The top panels of Fig. 4 compare the observed Lyα surface brightness profile (in erg s^{-1} cm^{-2} arcsec^{-2}) of Steidel et al. (2011) with the 'predicted' surface brightness profiles obtained from the Monte Carlo (filled black circles) and analytic (green solid lines) calculations for models I–III. These figures show clearly that none of the models can reproduce the observations: all three models have too much flux coming from $\theta < 2$ arcsec, although the actual observations also show a significant excess over the exponential fitting function at these impact parameters. This difference can be reduced by including dust (see Section 5.2). The most important difference, however, is at large impact parameters ($\theta \gtrsim 5$ arcsec or $b \gtrsim 40$ kpc), where *our predicted surface brightness profiles are low by an order of magnitude*.

The fact that our model surface brightness profiles are so much fainter is easy to understand: the central lower panel of Fig. 2 shows that at $r > 10$ kpc, the cold clouds are moving away from the central Lyα source at $v_c \gtrsim 600\,{\rm km\,s^{-1}}$. The majority (95 per cent) of Lyα photons will therefore enter the clumps with an apparent redshift of $\Delta v = 600 \pm 2\sigma = 300$–$900\,{\rm km\,s^{-1}}$. In order for the clouds to be

[11] The conversion $L_\alpha = 10^{42} \times [{\rm SFR}/({\rm M_\odot\,yr^{-1}})]$ applies for a Salpeter stellar initial mass function (IMF) and solar metallicities. We expect a larger Lyα luminosity at fixed SFR at lower gas metallicities (Schaerer 2003). For a Chabrier IMF – and again solar metallicity – we expect ∼1.8 times more Lyα luminosity at a given SFR (Steidel et al. 2010). It may therefore be possible to get the same Lyα luminosity from the central source if the escape fraction is $f_{\rm esc} \sim 50$ per cent, which is still large.

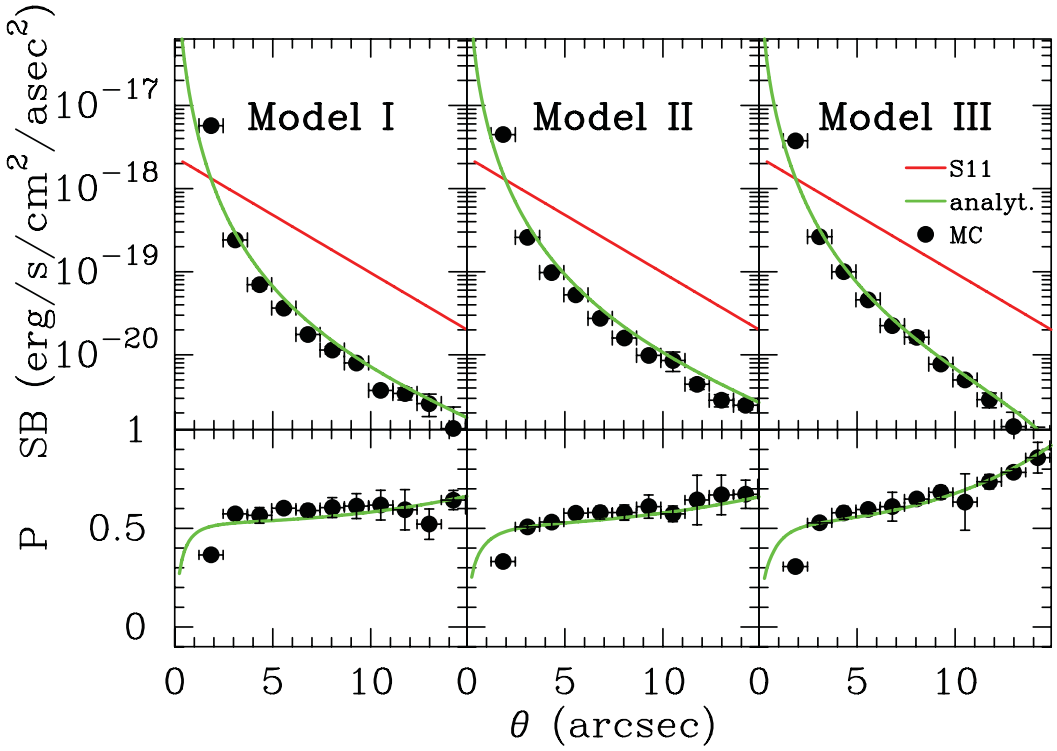

Figure 4. This figure shows a comparison between the 'predicted' and observed Lyα line profiles for our three models. The red solid lines show the surface brightness profile that was observed by Steidel et al. (2011). The solid green lines show the surface brightness profiles as given by equation (12) which assumes that photons scatter only once. The filled black circles show the results from our Monte Carlo calculations. This figure shows that the scattered Lyα radiation in our models gives rise to Lyα haloes that are more compact (i.e. centrally concentrated) and fainter by approximately an order of magnitude at $\theta \gtrsim 5$ arcsec. The lower panel shows the linear polarization as a function of impact parameter. We find that scattering through clumpy outflows can give rise to high levels of polarization. This figure also shows that there is very good agreement between our analytic and Monte Carlo calculations, which is a consequence of the fact that photons typically scatter in only one clump (or none at all).

opaque ($\tau > 1$) to Lyα photons, we must have $N_{\rm H\,I} \sim 3 \times 10^{19}$–$3 \times 10^{20}\,{\rm cm}^{-2}$. For most of our models, this requirement is met. However, the observed Lyα absorption line strength at $b = 30\,{\rm kpc}$ (see e.g. Fig. 1) is ${\rm EW}_{\rm obs}(b = 30\,{\rm kpc}) \sim 2$ Å, which is smaller than the absorption equivalent that would be produced by a single clump with this H I column density. The number of such clumps along the line of sight is therefore small (of the order of unity; see the lower-right panel of Fig. 2), and because the radii of the clumps $R_{\rm c} \ll r$, *the majority of photons escape from the CGM without encountering the outflowing, cold clumps.*

This last point is also illustrated nicely by the fraction of photons that never scatter in the outflow, denoted by $f_{\rm ns}$: in model I we find that $f_{\rm ns} \sim 0.75$, i.e. the majority of photons do not scatter off the cold clumps that give rise to the observed absorption. For model II, we have $f_{\rm ns} \sim 0.80$, while for model III we have $f_{\rm ns} = 0.43$. An immediate implication of this finding is that the photons that do not scatter should be observed as a Lyα point source of equal or larger luminosity than that of the Lyα halo. In the observations, the luminosity of the Lyα halo exceeds that of the central source by about a factor of ∼5, also in disagreement with our model.

Those photons that do scatter in the outflow get Doppler boosted to lower frequencies after they escape from the clump. The probability that the photon scatters in a second clump is then reduced further, because they appear even further from line resonance in the frame of the other clumps. Indeed, we find in the Monte Carlo simulations that photons generally scatter only in one clump, and this is the reason why our analytic solutions for the surface brightness profiles closely matches the ones we obtained with the Monte Carlo method.[12] The lower panels show that the scattered Lyα radiation is highly polarized, with the linear polarization $\mathcal{P} \gtrsim 40$ per cent at $S \lesssim 10^{-18}\,{\rm erg\,s^{-1}\,cm^{-2}\,arcsec^{-2}}$. This high level of polarization is another consequence of the fact that the photons typically scatter only once.[13]

[12] We stress that we do not expect perfect agreement, mostly because of the following: (i) in our dust-free Monte Carlo calculations the total flux of Lyα photons through each radial shell is conserved (but redistributed along the frequency axis), while this is not the case for the analytic calculations; (ii) the analytic formulation does not properly account for radiative transfer effects inside the clump where the photon scatters; (iii) we construct images that contain pixels that are $5 \times 5\,{\rm kpc}^2$ on a side, and binning is involved when creating azimuthally averaged surface brightness profiles.

[13] The H I column density of clumps $N_{\rm H\,I} \gtrsim 10^{21}\,{\rm cm}^{-2}$ at $r \lesssim 10\,{\rm kpc}$. Photons typically scatter several times on the surface of these clumps before escaping from them. This suppressed our the polarization signal that we predict with the Monte Carlo calculations at small impact parameters. We do not completely 'wash out' the polarization signature because polarization measures the anisotropy in the local Lyα radiation field weighted by the photons' escape probabilities. This can lead to significant levels of polarization despite the fact that photons can scatter multiple times (also see Dijkstra & Loeb 2008a).

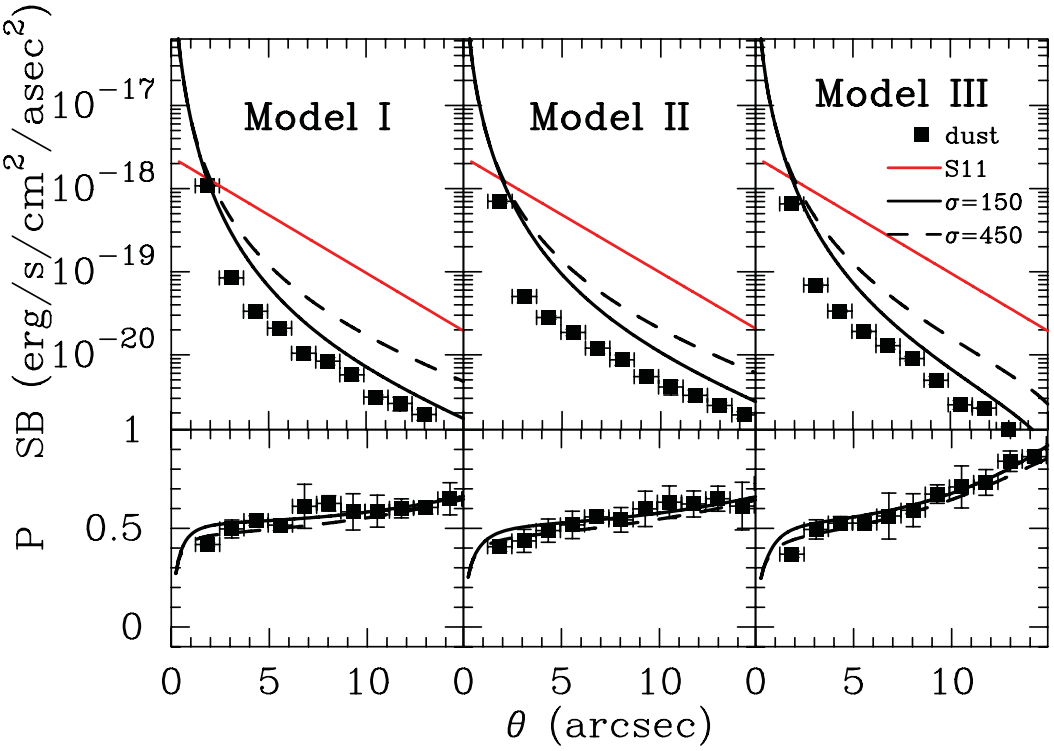

Figure 5. Same as Fig. 4. Here, we include models in which we assumed the initial Lyα line profile to be broader by a factor of 3, i.e. $\sigma = 450\,\mathrm{km\,s^{-1}}$. The resulting surface brightness profiles and polarization profiles are shown as the black dashed lines. We have shown results from our analytic calculations only. These plots show that significant (and probably unrealistic, see text) broadening of the initial line profile increases the surface brightness level of the scattered Lyα haloes, but not nearly enough to account for the observed Lyα halo profiles. The filled black squares show the result of models in which we include (a generous amount of) dust. Dust affects the inner regions of the surface brightness profiles most strongly.

Fig. 5 shows how our predicted surface brightness profiles change when we increase the width of the Lyα spectral line of the central source by a factor of 3 to $\sigma = 450\,\mathrm{km\,s^{-1}}$. Increasing the line width enhances the fraction of photons that enter the outflow with a significant blueshift. These photons appear closer to the line resonance in the frame of the outflowing gas, and are therefore more likely scattered. These plots show that broadening the initial line profile increases the surface brightness level of the scattered Lyα haloes, but not nearly enough to account for the observed Lyα halo profiles. Choosing even broader lines would clearly increase the surface brightness of the Lyα haloes more, but this choice would probably be unphysical. Scattering of Lyα photons through large columns of interstellar H I gas ($N_{\rm H\,I} \gtrsim 10^{21}\,\mathrm{cm^{-2}}$) could in theory easily broaden the line even more than this, but the line broadening as a result of scattering is limited by dust in the ISM (and its distribution; see fig. 8 of Laursen et al. 2009). Moreover, H I column densities of this magnitude would efficiently trap Lyα radiation. The radiation pressure exerted by this trapped radiation can cause the H I gas to expand outwards (Dijkstra & Loeb 2008a). Scattering of Lyα photons by this outflowing gas would not only broaden, but also redshift the line (e.g. Ahn & Lee 2002; Verhamme et al. 2006; Verhamme et al. 2008). Especially for H I column density of $N_{\rm H\,I} \sim 10^{21}\,\mathrm{cm^{-2}}$, this redshift can be large even for outflow velocities of only a few tens of $\mathrm{km\,s^{-1}}$. These redshifted Lyα photons would appear further from resonance in the frame of the cold clumps, and they would less likely be scattered. We therefore think that our choice $\sigma = 450\,\mathrm{km\,s^{-1}}$ corresponds to a reasonable upper limit on the amount of line broadening that occurs in the ISM. Finally, the filled black squares show that the predicted surface profiles are affected most strongly by dust in the central regions (see Section 5.2).

The fundamental reason why we fail to reproduce the observed Lyα haloes is that the clumps at large radii are moving away from the Lyα source too fast, thus requiring prohibitively large H I column densities in order to remain opaque to the Lyα photons. In Section 6.1 we explore a class of models for which the cold clumps decelerate after some radius, as expected naturally in models of momentum-driven winds.

5.2 Dusty clumpy outflows

In all models, the central clumps have the largest column densities. If the dust opacity of the clumps scales with their H I column density, then we can suppress the observed flux from the central regions. We can therefore 'flatten' the predicted surface brightness profile by adding dust to the clumps. We investigate this in more detail here. We rerun models I–III but add dust to clumps. The total amount of dust in a clump is normalized such that average dust absorption optical depth through a clump is $\tau_{\rm dust,abs} \equiv k_{\rm dust} \times (N_{\rm H\,I}/10^{20}\,\mathrm{cm^{-2}})$, i.e. for a column density of $N_{\rm H\,I} = 10^{20}\,\mathrm{cm^{-2}}$, the total dust absorption opacity is $\tau_{\rm d} = k_{\rm dust}$. We will explore the impact of dust for $k_{\rm dust} = 1$. For comparison, the diffuse H I phase of the Milky Way has $k_{\rm dust} = 0.1$ (Hansen & Oh 2006, and references therein). We choose the larger value $k_{\rm dust} = 1$ to clearly illustrate the potential impact of dust. To maximize the impact of dust, we also assumed that the dust grains do not scatter Lyα photons (i.e. $A = 0$).

The black filled squares in Fig. 5 show the predicted surface brightness and polarization profiles in the presence of dust. We indeed find that the surface brightness profiles are suppressed most at small impact parameters. Also, the predicted polarization is affected very little. Note that for non-zero dust scattering albedo, the radiation that was scattered by dust would be unpolarized, which would lower the overall polarization. However, if the Lyα haloes were a result of scattering by dust grains, then we would expect the UV continuum to follow the same surface brightness profile, which is not observed (Steidel et al. 2011).

6 Lyα HALOES FOR MORE 'REALISTIC' MODELS

6.1 Model IV: adopting a more realistic velocity profile

In our previous models, the cold clouds accelerate as they break out of the ISM. The acceleration decreased with radius as $a_c(r) \propto r^{-\alpha}$, where $\alpha = 1.4$–1.5 in models I–III. This continuous acceleration represents a 'momentum-driven' wind scenario in which the cloud's acceleration is driven by, for example, ram pressure of the hot wind or radiation pressure. However, galaxies populate the centres of gravitational wells, and the cold clumps are subject to a gravitational force which decreases as $\propto r^{-1}$ in the potential of an isothermal sphere. The deceleration of clumps as a result of gravity therefore decreases slower with radius than $a_c(r)$, and gravity dominates beyond some 'transition' radius $r_{\rm trans}$. This deceleration following acceleration occurs for any model in which $\alpha > 1$. This deceleration potentially has important implications for the predicted surface brightness profiles of the Lyα haloes: one of the main reasons models I–III significantly underpredict the Lyα surface brightness is that the clumps were receding from the Lyα source too rapidly (see Section 5.1).

The goal of this section is to investigate whether we can reproduce the absorption-line and Lyα halo data better in simplified models which take this gravitational deceleration of the cold clumps into account. Following Murray, Quataert & Thompson (2005; also see Martin 2005) we write the momentum equation for a cold, optically thick, clump as

$$\frac{{\rm d}v_c}{{\rm d}t} = -\frac{GM(r)}{r^2} + Ar^{-\alpha}, \qquad (13)$$

where we used the same function to describe the cloud acceleration as before (Section 3.1). The case $\alpha = 2$, $A = 2\sigma^2 R_g$ corresponds to equation (24) of Murray et al. (2005). Here, $R_g \equiv r_{\rm min}(L/L_{\rm edd})$, where the ratio $L/L_{\rm edd}$ denotes the total luminosity of the source normalized to the Eddington luminosity of the galaxy (see Murray et al. 2005, for details). Following Murray et al. (2005) we take for the model of the gravitational potential that of an isothermal sphere for which $M(r) = 2\sigma^2 r/G$, in which σ denotes the velocity dispersion.

The solution to equation (13) is given by

$$v_c(r) = 2\sigma\sqrt{\ln\left(\frac{r_{\rm min}}{r}\right) + \frac{A}{2\sigma^2(1-\alpha)}\left(r^{1-\alpha} - r_{\rm min}^{1-\alpha}\right)}, \qquad (14)$$

where we assumed the boundary condition $v_c(r_{\rm min}) = 0$.

In theory, it is straightforward to repeat the analysis of Section 3.1, and do a MCMC simulation to simultaneously constrain all model parameters including $r_{\rm min}$, A and σ by finding the best-fitting model to the absorption-line data. We have instead fixed the values $\alpha = 1.4$, $r_{\rm min} = 1$ kpc, which we found to provide good fits for models I–III. We also assumed $\sigma = 150\,{\rm km\,s^{-1}}$, which is the value that we assumed previously (see Section 5) and $R_g = 2.5$ (i.e. $A = 5\sigma^2$). This latter choice is entirely empirical: the dot–dashed line in Fig. 6 shows that the resulting velocity profile (equation 14) reaches a maximum of $v_{c,\rm max} \sim 350\,{\rm km\,s^{-1}}$ at $r \sim 10$ kpc and then decreases to $v_c \sim 100\,{\rm km\,s^{-1}}$ at $r = 250$ kpc. For smaller values of R_g, the clumps would turn around and fall back on to the galaxy, while larger values of R_g would result in negligible deceleration. The solid line shows the velocity profile that was adopted in model I.

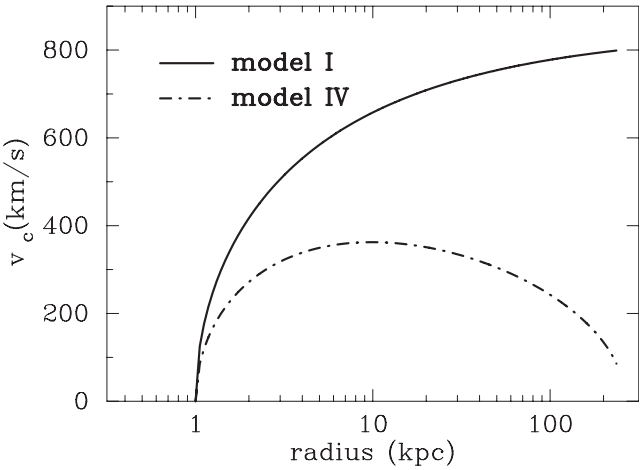

Figure 6. This plot shows the velocity profiles that we adopt for model I (solid line) and model IV (dot–dashed line). In contrast to model I, in model IV gravity causes the clumps to decelerate beyond some critical radius $r_{\rm crit}$. As a result, clumps flow out at lower velocities in model IV, which makes them more opaque to Lyα photons, which results in brighter Lyα haloes (text).

The MCMC finds the best-fitting model for the parameters shown in Table 2. This model – which we refer to as model IV – is compared to the absorption-line data in the left-hand panel of Fig. 7. The right-hand panel of Fig. 7 shows the predicted Lyα surface brightness and polarization profiles. It is clear that the predicted surface brightness is significantly higher than that predicted by models I–III and agrees with the data to within a factor of $\sim$2–3. The enhanced surface brightness profile is a direct result of the lower outflow velocity of the clumps which makes them more opaque to Lyα photons. The photons still most often scatter off one clump, and the analytic calculation still compares quite well to the result we obtained from the Monte Carlo simulation. The predicted polarization is also high for this model, with the linear polarization reaching $P \sim 40$ per cent at a surface brightness (SB) level of SB $\sim 10^{-18}\,{\rm erg\,s^{-1}\,cm^{-2}\,arcsec^{-2}}$.

Importantly, this model still predicts that $f_{\rm ns} \sim 60$ per cent of the photons does not scatter at all in the outflow. This model therefore also predicts that the Lyα halo is accompanied by a point source of comparable luminosity, which is not observed.

6.2 Model V: concentrating the outflow into cones

The final model that we consider – which we refer to as model V – is a biconical outflow model, in which the hot and cold gas escape from the galaxy along two cones whose axes are parallel. The reason that we study such a model is the observed azimuthal dependence of the Mg II at $b < 50$ kpc of inclined disc-dominated galaxies at $z = 0.5$–0.9, which indicates the presence of biconical outflows that are aligned along the disc rotation axis (Bordoloi et al.

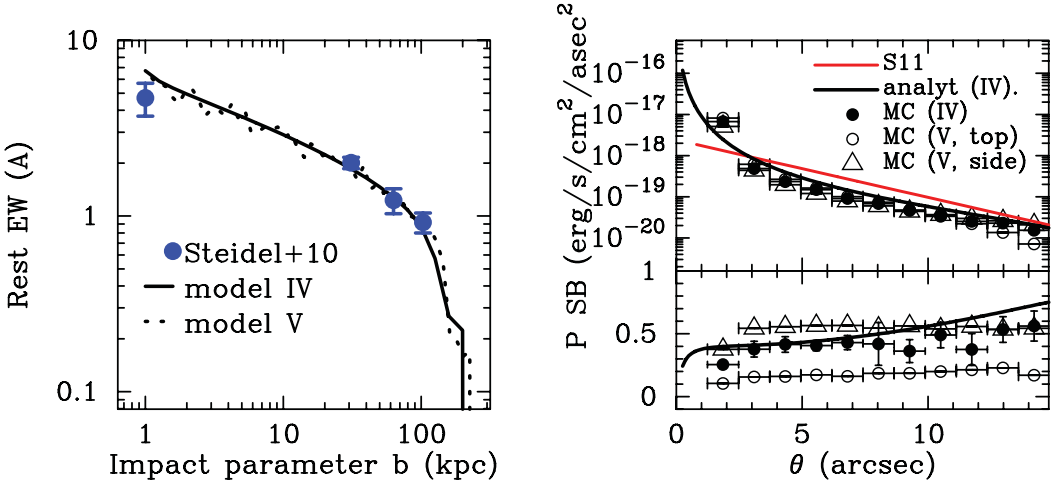

Figure 7. The left-hand panel shows the predicted absorption line strength as a function of impact parameter for model IV, while the right-hand panel shows the predicted Lyα surface brightness profiles as obtained from the Monte Carlo simulation (black filled circles), and analytic calculation (black dashed line). This model – in which gravity decelerates the cold clumps after their initial acceleration – clearly predicts a surface brightness profile that is much closer to the observations than models I–III.

2011). We would like to see how our results change if we drop the assumption of having symmetric outflows.

We take the parameters from model IV but now compress the outflowing clumps into two cones. For simplicity we align the cone axes with the z-axis, and assume that the opening angle is $\theta = 45^\circ$ (i.e. the edge of the cone intersect the z-axis at 45°). This compression of the outflow has two implications: (i) the number density of cold clumps is enhanced by a factor of $1/[1-\cos\theta] \sim 3.5$ at each radius and (ii) the pressure of the hot wind also increases by a factor of 3.5, which compresses the radius of the cold clouds by a factor of $3.5^{1/3} = 1.5$. The dotted line in the left-hand panel of Fig. 7 shows the predicted EW versus b curve for a random realization of model V. This model also nicely reproduces the observations without any further tuning. We have not performed an analytic calculation of EW as a function of b (as in equation 7), as this would require averaging over random cone orientations.

Fig. 8 shows surface brightness contours for model V when we view the outflow along the cone axis (left-hand panel), and perpendicular to the cone axis (right-hand panel). The black/red/blue contour indicates a surface brightness level of $\log[\mathrm{SB}/(\mathrm{erg\ s^{-1}\ cm^{-2}\ arcsec^{-2}})] = -18.0/-19.0/-20.0$. This figure illustrates that our code works on non-spherical clump distributions. For this calculation, we assume that all Lyα photons escape from the galaxy into the cones (i.e. the central source does not emit Lyα photons isotropically, but instead into two cones with opening angles of 45°), which is motivated by the physical picture in which the outflow has 'cleared' out a cone of lower H I column density along which Lyα photons escape. Studies of Lyα transfer through simulated galaxies have also shown that the escape of Lyα photons from the dusty ISM of galaxies can proceed highly anisotropically: the Lyα flux transmitted into different directions may vary by an order of magnitude (Laursen et al. 2009; Yajima et al. 2012b).

The right-hand panel of Fig. 7 shows the predicted azimuthally averaged surface brightness and polarization profiles when the bipolar outflow is viewed from the top (open circles) and from the side (open triangles). The predicted polarization is lower (higher) when we view the outflow from the top (side), as photons typically scatter by $\mu < \cos 45^\circ$ ($\mu > \cos 45^\circ$). This panel also shows that the azimuthally averaged surface brightness profile depends only weakly on whether the outflow is bipolar or not, and on from which angle

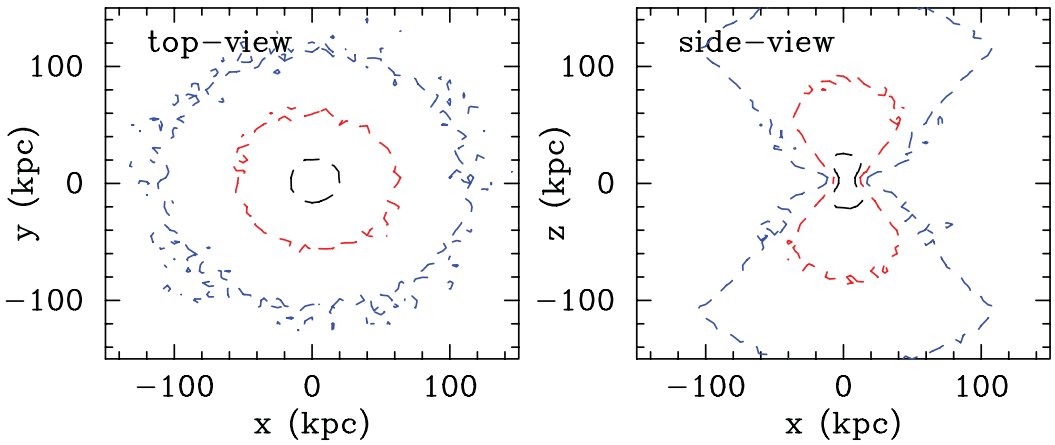

Figure 8. This figure shows surface brightness contours for a biconical outflow model as seen along the axis of the cone (left-hand panel) and perpendicular to the cone axis (right-hand panel). The black/red/blue contour denotes a surface brightness level of $\log[\mathrm{SB}/(\mathrm{erg\ s^{-1}\ cm^{-2}\ arcsec^{-2}})] = -18.0/-19.0/-20.0$. The opening angle of the cone is 90°. This plot illustrates a case in which our code works on non-spherical clump distributions.

we view the outflow. This last result is important as it can alleviate the problem that model IV has, namely that ∼50 per cent of all Lyα photons do not scatter in the outflow, and should thus be detectable as a Lyα source. Invoking this bipolarity may help us avoid predicting a Lyα point source with Lyα haloes, because when $\theta = 45^\circ$, a fraction $\cos\theta \sim 0.71$ of all the sightlines would not lie in the cone, and we would not see a point source along these sightlines.

Two caveats to model V are the following: (i) as mentioned and justified above, our model assumes that Lyα photons escape from the galaxy into the cones of outflowing gas. This 'focusing' of Lyα photons into the biconical outflow requires additional H I gas which is not present in our model. This gas would contribute to the measured EW at $b = 0$, and would hence reduce the amount of H I gas that we are allowed to assign to the clumps at small impact parameters. This reduced amount of cold gas would suppress the predicted amount of scattering – and hence the predicted surface brightness – at small impact parameters (which would agree better with the data); (ii) if the outflowing material were indeed all confined to two cones with opening angles $\theta = 45^\circ$, then we fail to explain why blueshifted absorption lines of low-ionization absorption lines are observed in practically all sightlines (e.g. Shapley et al. 2003; Steidel et al. 2010). We intend to include the additional constraints provided by the 'down-the-barrel spectra' in a more realistic model of the outflows, in which the clump distribution is a function not only of radius r, but also of azimuthal angle (see Section 7.4).

7 DISCUSSION

7.1 Discussion of model uncertainties and caveats

Here, we discuss potential implications of our adopted assumptions and simplifications.

(i) We constrain the H I content of the cold clumps in the large-scale outflow with the mean observed absorption line strength (EW) as a function of impact parameter (b). These same clumps scatter Lyα photons emitted by the foreground galaxy into the line of sight, which could weaken the observed line strength (see Prochaska, Kasen & Rubin 2011). For example, the observed surface brightness at $b = 31$ kpc is 6×10^{-19} erg s^{-1} cm^{-2} arcsec^{-2}. The Lyα absorption strength has been measured over an area of 1.2×1.35 arcsec^2 (C. Steidel, private communication), which implies that the observed absorption is accompanied by $\sim 10^{-18}$ erg s^{-1} cm^{-2} of scattered radiation.

We can compare this scattered flux to the flux that has been absorbed out of the spectrum of the background galaxy as follows: (i) the observed flux density (f_λ in erg s^{-1} Å^{-1}) at rest frame $\lambda = 1100$ Å is comparable to that at $\lambda = 1500$ Å (see fig. 5 of Steidel et al. 2010, and use $f_\nu \propto \lambda^2 f_\lambda$); (ii) we estimate the observed rest-frame flux density at $\lambda = 1500$ Å (rest frame) from the average UV-derived SFR, uncorrected for dust, which was SFR $= 8\,M_\odot$ yr^{-1} assuming the Kennicutt (1998) star formation calibrator (Erb et al. 2006). For a galaxy at $z = 2.3$ this SFR translates into an observed rest frame $f_\lambda(\lambda = 1500\,\text{Å}) \sim 2 \times 10^{-18}$ erg s^{-1} cm^{-2} Å^{-1}. After combining (i) and (ii), we find that the scattered flux of $\sim 10^{-18}$ erg s^{-1} cm^{-2} corresponds to a rest-frame EW ~ 0.5 Å, which lies a factor of 4 below the measured EW. This implies that scattered flux is subdominant to the absorbed flux. At larger impact parameters the scattered flux becomes exponentially fainter and even less important.

Obviously, our calculation is approximate and relies on an average spectrum, an average SFR and a median redshift. In certain cases, we expect the scattered flux to be more important than our previous estimate. However, in such cases the spatially extended scattered flux is detectable in spectra of pixels adjacent to the background galaxy, and can be corrected for. We therefore conclude that the potential contribution of scattered radiation to the observed EW does not affect our results.

(ii) When constraining the H I content of the clumps (using the observed EW as a function of b), we implicitly assume that only the cold clumps in the outflow contribute to the observed EW. However, van de Voort et al. (2012) have recently found that in their hydrodynamical simulations, the cold streams of gas that are feeding the central galaxy may produce more large column density absorbers ($N_{\rm H\,I} \gtrsim 10^{20}$ cm^{-2}) around galaxies than outflows (also see Fumagalli et al. 2011, but note that modelling the outflowing component at large impact parameter is extremely uncertain, see Section 3). The probable contribution of cold streams to the observed EW at a given impact parameter reduces the amount of H I that we can assign to cold clumps in the outflow. With less H I in the outflowing clumps, we expect them to scatter fewer Lyα photons, and that consequently our surface brightness levels are reduced by an amount which depends on the overall contribution of the outflowing cold clumps to the observed EW at a given b.

(iii) The observed EW as a function of b has been measured around galaxies with a mean redshift $\langle z \rangle = 2.2$ (Steidel et al. 2010), while the mean redshift of galaxies that were used in the stack of narrow-band images was $\langle z_{\rm halo} \rangle = 2.65$. While galaxies in both samples were selected in very similar ways, and therefore likely trace similar populations (e.g. both populations have virtually identical mean SFRs, see Section 3.1), the observed Lyα absorption line strength does not really probe the same gas that is scattering the Lyα haloes. For this reason, we consider differences between the predicted and observed Lyα surface brightness profiles at the factor of 2–3 level (as was the case in model IV) not a problem. On the other hand, it is unrealistic to attribute the order of magnitude differences in the predicted surface brightness profiles (which we found for models I–III) to selection effects.

(iv) In our model in which the clumps decelerate after their initial acceleration (see Section 6.1), the clumps reach a maximum velocity of $v_{\rm c,max} \sim 350$ km s^{-1}, which is well below the maximum velocity that was inferred by Steidel et al. (2010) of $v_{\rm max} \sim 800$ km s^{-1}. Fujita et al. (2009) found in their hydrodynamical simulations that a small fraction of the cold shell fragments could be accelerated to reach large outflow velocities ($\gtrsim$750 km s^{-1}), while the bulk of the gas was travelling at lower velocities of ∼300 km s^{-1}. This suggests that the maximum velocity that is inferred from the observations can be consistent with our model which only describes the kinematics of this bulk of the gas. Furthermore, because of the large H I column densities in the clumps, the photons can scatter in the wings of the Lyα line profile. As a result, Lyα absorption may trace a wider range of velocities than the range of actual outflow velocities.

(v) In our model there is a one-to-one mapping between radius and velocity. In reality, we expect outflows to have a range of velocities at a given radius: for example, in the model of Martin (2005), the cloud acceleration increases with their H I column density. For a range of H I column densities we therefore expect the cold clouds to have a range of velocities at a given radius. This scatter may boost the predicted Lyα surface brightness profile, in particular when this scatter gives rise to a population of clumps with a lower $v_{\rm c}(r)$.

(vi) Our model assumes that there is a unique clump mass. In reality, there is a distribution. This is very likely not an issue: in model I the clump mass was $m_{\rm clump} \sim 10^4\,M_\odot$, while in model II the clump mass was ∼10 times larger. As long as the distribution of clumps is constrained by the absorption-line data, we predicted

virtually identical surface brightness profiles. We therefore consider it unlikely that we obtain significantly different surface brightness profile, if we assume a finite range of clump masses.

(vii) Our model assumes a Gaussian emission profile, for which the width is set by the velocity dispersion of the gas. However, the outflow contains swept-up shells of cold neutral gas before it breaks out of the galaxy. It is therefore not unlikely that Lyα photons scatter off these dense cold shells, which would result in an overall redshift of the line, *before the Lyα photons escape from the galaxy into the large-scale outflow*. Redshifting of the Lyα line would reduce the overall scattering probability in the outflow, and could reduce the predicted surface brightness profiles.

(viii) We assumed that the escape fraction[14] of Lyα photons was 50–100 per cent (depending on the choice of IMF, and gas metallicity as these affect the *intrinsic* Lyα luminosity of the galaxy at a fixed SFR). This potentially high escape fraction was already noted by Steidel et al. (2011). In our models, it is required to be higher by a factor of ∼2 because about half of the photons that escape from the galaxy into the large-scale outflow were *not* scattered at all and are effectively wasted.

This radiation that is not scattered in the outflow must be a point source of comparable (model IV) or higher (models I–III) luminosity than the halo itself, which is in conflict with observations. This disagreement can be alleviated by invoking that the outflow is bipolar (see Section 6.2), and/or by a population of low column density absorbers (as observed in galaxy–quasar pair data by Rudie et al. 2012) that have a velocity v_c that differs substantially from that in of the clumps in models I–V (see Section 7.3).

7.2 Connection with Lyα blobs

Steidel et al. (2011) found the Lyα 'blobs' – defined loosely as having an area $\gtrsim$16 arcsec^{-2} for which SB $\gtrsim 10^{-18}$ erg s^{-1} cm^{-2} arcsec^{-2} (Matsuda et al. 2004; also see Steidel et al. 2000; Saito et al. 2006) – within their narrow-band survey volume to have surface brightness profiles almost identical to that of the Lyα haloes, apart from an overall off-set in their overall normalization. Scattering of Lyα photons in a large-scale outflow can theoretically explain Lyα blobs if we increase the SFR of the central Lyα source. This is illustrated in Fig. 9, which shows the dependence of the predicted surface brightness profile on SFR for model IV (which was also shown in Fig. 7). In these calculations we kept all other model parameters fixed.

The dashed line shows the original prediction for model IV which assumed SFR = 34 M$_\odot$ yr^{-1}. The dotted line/dot–dashed line shows the predicted surface brightness profile for SFR = 100 M$_\odot$ yr^{-1}/ SFR = 10 M$_\odot$ yr^{-1}. The predicted surface brightness profile depends quite strongly on SFR. This is because (i) the intrinsic Lyα luminosity of the central source scales linearly with SFR and (ii) the amount of cold gas that can scatter the Lyα photons also depends linearly on SFR. These two effects combined suggest that the surface brightness at a given impact parameter can depend on SFR as $\propto$ SFR^2, which can explain that the surface brightness at a given impact parameter can vary by an order of magnitude as a result of a factor of ∼3 change on the SFR (which gives more weight to the contribution of high-SFR galaxies to the stacked Lyα image). The feature in the SFR = 10 M$_\odot$ yr^{-1} curve at $\theta \sim 9$ arcsec reflects that the clumps do not self-shield at $r \gtrsim 76$ kpc in this model.

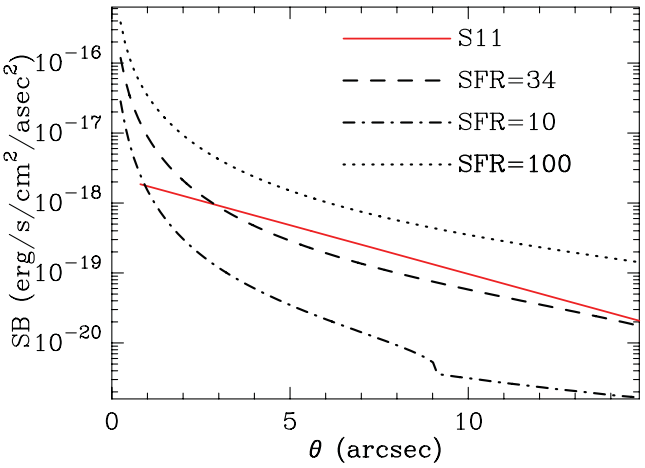

Figure 9. This plot shows the dependence of our surface brightness profiles of the Lyα haloes, as a function of the SFR (in M$_\odot$ yr^{-1}), assuming the same model parameters for the outflow (mass loading factor, number of clumps, etc.). The predicted surface brightness profile depends strongly on SFR because (i) the intrinsic Lyα luminosity of the central source scales linearly with SFR and (ii) the total amount of scattering material scales linearly with SFR. As a result, changing SFR by a factor of ∼3 can change the surface brightness at a fixed θ by an order of magnitude.

Fig. 9 shows that it is possible to have Lyα blobs around galaxies that are forming stars at a rate SFR $\gtrsim$ 100 M$_\odot$ yr^{-1}, as the predicted surface brightness profile drops below ∼10^{-18} erg s^{-1} cm^{-2} arcsec^{-2} only at $\theta \gtrsim$ 7–8 arcsec. There is observational evidence that a fraction of the Lyα blobs are associated with submm galaxies, which are believed to be forming stars at rates of SFR ∼ 10^3 M$_\odot$ yr^{-1} (Chapman et al. 2001; Geach et al. 2005, 2007; Matsuda et al. 2007). Chapman et al. (2005) have noted that a remarkably high fraction (∼50 per cent) of submm galaxies show Lyα emission lines in their spectra (also see Nilsson & Møller 2009, for a detection of Lyα from a ULIRG). This may indeed suggest that enough Lyα photons escape from the dusty interstellar media of submm galaxies, and then scatter in the large-scale outflow to account for the blobs. Support for the notion that Lyα blobs consist of scattered radiation is provided by the detection of polarization by Hayes, Scarlata & Siana (2011a), albeit at a level that is lower by a factor of ∼2 than the values predicted here. On the other hand, Prescott et al. (2011) put an upper limit on $P \lesssim 10$ per cent in LABd05 (Dey et al. 2005), which clearly rules out our models.

It appears increasingly plausible that there are distinct physical mechanisms that power Lyα blobs. The polarization measurement of Hayes et al. (2011a) clearly favours models that invoke scattering. On the other hand, Prescott et al. (2012) find that the UV continuum (non-ionizing) associated with LABd05 is also spatially extended, which favours having spatially extended emission of both UV and Lyα photons. This observation could be consistent with *dust scattering*, which would explain why the polarization of Lyα would not have been detected (see Section 4.1). However, given the large observed EW of the diffuse Lyα when measured relative to the diffuse UV continuum (restframe EW $\gg$ 200 Å; Prescott et al. 2012), this is not very plausible. Alternative support for the notion that some blobs are not a result of scattering is provided by those blobs that

[14] This escape fraction refers to the fraction of photons that escape from the ISM of the galaxy into the large-scale outflow. This escape fraction differs from the escape fraction that is used in recent observational papers (e.g. Hayes et al. 2010, 2011b; Blanc et al. 2011), which represents the ratio of the observed to the intrinsic Lyα flux, which can depend sensitively on the surface brightness threshold of the observations (Zheng et al. 2010; also see Jeeson-Daniel et al. 2012).

do not have any clear galaxy counterparts (e.g. Nilsson et al. 2006; Smith & Jarvis 2007).

7.3 Additional constrains from galaxy–quasar pair data

Rakic et al. (2012) and Rudie et al. (2012) use galaxy–quasar pairs to probe the CGM of the foreground galaxies. Rudie et al. (2012) present 10 pairs for which the background quasar lies at $b < 100$ kpc. They find six absorbers with $\log N_{\rm H\,I} \gtrsim 17.0$, of which two absorbers have $\log N_{\rm H\,I} \gtrsim 18.0$, of which one absorber has $\log N_{\rm H\,I} \sim 20$. We compare this to model V at $b = 71$ kpc, which corresponds to the median value for b if the sightlines are distributed randomly within the circle for radius $b = 100$ kpc. We find that our model predicts $\sim$7 absorbers with $\log N_{\rm H\,I} \gtrsim 17.0$, of which $\sim$7 have $\log N_{\rm H\,I} \gtrsim 18.0$, of which $\lesssim$1 absorber has $\log N_{\rm H\,I} \gtrsim 19.3$. Given the simplified nature of our model, and the relatively small number of observed sightlines, we consider these numbers encouraging. For example, our predicted number of absorbers with $\log N_{\rm H\,I} \gtrsim 18.0$ is reduced to $\sim$3, and therefore more consistent with observations, if we simply increase the critical number density above which gas self-shields by a factor of 2 to $n_{\rm crit} = 0.012\,{\rm cm}^{-3}$, which is still reasonable [e.g. Faucher-Giguère et al. (2010) adopt $n_{\rm crit} = 0.01\,{\rm cm}^{-3}$]. Such a modification reduces the predicted EW as a function of b, but only significantly at $b \gtrsim 70$ kpc. In this case the observed EW at $b = 100$ kpc could be accounted for by a large number of lower column density absorbers, which have been observed (see below) but which are not present in the model.

Another difference worth emphasizing is that our model predicts that 10 sightlines with $b = 71$ kpc should intersect a total of $\sim$13 cold clumps. Rudie et al. (2012) find significantly more low column density, $\log N_{\rm H\,I} = 14.5$–17.0, absorbers. This implies that our clumpy outflow model does not account for all the observed absorbers, and thus all potential 'scatterers'. However, if we wish to use low column density absorbers to scatter photons into Lyα haloes, then they must have lower outflow velocities (or they have to be inflowing) than the clumps in our model, otherwise they are transparent to the Lyα photons. The possible presence of these low column density absorbers that move at different velocities than the high column density clumps in our models may have the interesting benefit that they reduce the fraction of photons that do not scatter in the outflow at all. These clumps may thus reduce the luminosity of the central Lyα sources that accompanies the Lyα haloes in models I–IV, and in model V when we view the outflow down one of the cones.

7.4 Outlook and potential improvements

In Section 7.1 we highlighted the simplifications of our model, which underlined that many improvements are possible. We discuss some examples of how we intend to improve upon our analysis below.

We have so far focused on using the observed Lyα absorption line strengths as well as the surface brightness profile of Lyα haloes to constrain parameters of outflow models. However, there is information encoded in the observed spectral line shape of the Lyα emission line, as well as whether it is redshifted or blueshifted relative to the galaxies' systemic velocity (e.g. Yamada et al. 2012 and references therein). For example, Lyα lines that are blueshifted/redshifted with respect to the systemic velocity – to first order – are indicative of scattering through an opaque inflowing/outflowing medium (e.g. Zheng & Miralda-Escudé 2002; Dijkstra et al. 2006). The first joint Hα–Lyα spectral line observations of spatially extended Lyα nebulae (Yang et al. 2011), compact Lyα-selected galaxies (Finkelstein et al. 2011; also see McLinden et al. 2011, for joint Lyα–[O III] observations) and 'double-peaked' Lyα-emitting UV-selected galaxies (Kulas et al. 2012) have recently been reported. Kulas et al. (2012) have already shown that such observations can rule out the 'shell models' for outflows. In future we plan to explore what additional constraints we can place on outflow models on small scales (i.e. $r \lesssim 10$ kpc) with observations of the Lyα spectral line shape (and shift). Finally, our previous discussion (Section 7.3) showed that observations of galaxy–quasar pairs (Rakic et al. 2012; Rudie et al. 2012) already provide useful additional constraints on our models.

We also plan to extend our study to include other lines. For example, Bordoloi et al. (2011) have presented the radially (and azimuthally) dependent absorption line strength of Mg II around bright flux-selected galaxies at $0.5 < z < 0.9$ from the zCOSMOS redshift survey. We can constrain the Mg II content of the clumps in our model by matching this data. We can then make predictions for surface brightness profiles of scattered Mg II emission, and compare them to observations of spatially extended Mg II emission around a $z = 0.69$ starburst galaxy (Rubin et al. 2011).

8 CONCLUSIONS

We have presented 'constrained' radiative transfer calculations of Lyα photons propagating through clumpy, dusty, large-scale outflows, and explore whether scattering through such an outflow can quantitatively explain the Lyα haloes that have been observed around LBGs (see Steidel et al. 2011). As part of our analysis we have modified a Lyα Monte Carlo radiative transfer code to allow us to follow the propagation of Lyα photons through a multiphase, dusty medium for arbitrary distributions of clumps. This code also computes the polarization of the scattered Lyα radiation. Previous calculations of the polarization of scattered Lyα radiation have focused only on homogeneous spherically symmetric gas clouds or shells. We have successfully tested our code against several analytic solutions, some of which – in particular the directional-dependent frequency redistribution function – are new.

Modelling the distribution and kinematics of cold gas in outflows from first principles is an extremely complex task, which likely requires magnetohydrodynamical simulations that have sub-pc resolution (Section 3). We have taken a different approach, and constructed phenomenological models for the large-scale outflows in which cold ($\log T_{\rm c} \sim 3$–4) clumps are in pressure equilibrium with a hot ($\log T_{\rm h} \sim 7$) wind. We first considered models in which the cold clumps are distributed symmetrically around the source, and which accelerate continuously as they break out of the ISM of the galaxy. Steidel et al. (2010) showed that this type of model may qualitatively simultaneously explain the observed Lyα absorption line strength in the CGM, as well as the observed surface brightness profiles of Lyα emission-line haloes.

Our more detailed analysis shows that such models – which contain 10^5–10^6 discrete clumps – can reproduce the observed Lyα absorption line strengths of the CGM measured in the spectra of background galaxies very well, and for model parameters that are physically plausible (see Fig. 1). However, when we insert a Lyα source in the centre of these clumpy outflow models, and compute the observable properties of the scattered Lyα radiation, we typically find that the predicted Lyα haloes are significantly fainter and more concentrated than what is observed (Fig. 4). The reason for this discrepancy is easy to understand: outflowing cold clumps that scatter photons at large ($b \gtrsim 30$ kpc) impact parameters are propagating away from the Lyα source at $v \gtrsim 600\,{\rm km\,s}^{-1}$.

In order for the clumps to scatter Lyα photons they must be opaque to these photons, which requires H I column densities in excess of $N_{\rm H\,I} \gtrsim 10^{19}\,{\rm cm}^{-2}$. However, the absorption-line data requires that the number of such clumps at large impact parameters is so small that a significant fraction of the photons never encounter them. Our conclusion that we cannot simultaneously fit the absorption line and Lyα halo data – with a clumpy outflow in which the clumps are distributed spherically around the galaxy and which accelerate with radius – is therefore robust.

We also found that the vast majority of photons scatter in zero or one clump and that it is possible to analytically compute the Lyα surface brightness and polarization profiles (see Fig. 4). The fact that a significant fraction of the photons do not scatter in the outflow is problematic. The photons that do not scatter must be detectable as a point source, and its predicted luminosity equals or exceeds the total luminosity of the Lyα halo, which is in further disagreement with the observations.

We can much better simultaneously reproduce the observed Lyα absorption line strengths and the Lyα haloes with models in which the cold outflowing clumps decelerate (see Fig. 7). This deceleration occurs naturally in models of momentum-driven winds (Section 6.1). We can alleviate the problem of predicting a bright Lyα point source to accompany the halo if the outflow is bipolar with a (half) opening angle $\theta \lesssim 45^\circ$ (Section 6.2). This problem may be further reduced if the observed additional low column density absorbers in galaxy–quasar pairs move at velocities that allow them to resonantly scatter an additional fraction of the Lyα photons (see Section 7.3).

We found that models which do fit both the absorption line strength and Lyα halo data give rise to levels of linear polarization that reach $P \sim 40$ per cent at a surface brightness level of SB $\sim 10^{-18}\,{\rm erg\,s^{-1}\,cm^{-2}\,arcsec^{-2}}$ (e.g. Fig. 7). This polarization signature is likely unique to the scattering models and likely distinguishes them from models in which the Lyα photons were emitted over a spatially extended region (see Section 1). Furthermore, because the large polarization signature is a result of non-resonant scattering, the polarization also distinguishes our models from those of Zheng et al. (2011b), in which the haloes were a result of resonant scattering (Section 1). It should be noted that it remains to be shown that predictions of these other models are in quantitative agreement with the observed Lyα absorption-line data, as well as the Lyα haloes.

This paper illustrates clearly that Lyα emission-line haloes around star-forming galaxies provide valuable constraints on the cold gas distribution and kinematics in their CGM, and that these constraints nicely complement those obtained from absorption-line studies alone.

ACKNOWLEDGMENTS

We thank Alice Shapley, Andrea Ferrara, Akila Jeeson-Daniel, Benedetta Ciardi, Evan Scannapieco and Rongmon Bordoloi for helpful discussions. We thank Charles Steidel for helpful correspondence, and Matthew Hayes and Moire Prescott for helpful comments on an earlier version of this paper. We thank an anonymous referee for a prompt report and for carefully reading our paper.

REFERENCES

Adams T. F., 1971, ApJ, 168, 575
Ahn S.-H., Lee H.-W., 2002, J. Korean Astron. Soc., 35, 175
Ahn S.-H., Lee H.-W., Lee H. M., 2000, J. Korean Astron. Soc., 33, 29
Barkana R., Loeb A., 2003, Nat, 421, 341
Barnes L. A., Haehnelt M. G., Tescari E., Viel M., 2011, MNRAS, 416, 1723
Blanc G. A. et al., 2011, ApJ, 736, 31
Bordoloi R. et al., 2011, ApJ, 743, 10
Cantalupo S., Porciani C., Lilly S. J., Miniati F., 2005, ApJ, 628, 61
Ceverino D., Klypin A., 2009, ApJ, 695, 292
Chapman S. C., Lewis G. F., Scott D., Richards E., Borys C., Steidel C. C., Adelberger K. L., Shapley A. E., 2001, ApJ, 548, L17
Chapman S. C., Blain A. W., Smail I., Ivison R. J., 2005, ApJ, 622, 772
Cooper J. L., Bicknell G. V., Sutherland R. S., Bland-Hawthorn J., 2008, ApJ, 674, 157
Dalla Vecchia C., Schaye J., 2008, MNRAS, 387, 1431
Davé R., Finlator K., Oppenheimer B. D., 2012, MNRAS, 421, 98
Dayal P., Ferrara A., 2012, MNRAS, 421, 2568
Dey A. et al., 2005, ApJ, 629, 654
Dijkstra M., Loeb A., 2008a, MNRAS, 386, 492
Dijkstra M., Loeb A., 2008b, MNRAS, 391, 457
Dijkstra M., Loeb A., 2009, MNRAS, 400, 1109
Dijkstra M., Wyithe J. S. B., 2010, MNRAS, 408, 352
Dijkstra M., Haiman Z., Spaans M., 2006, ApJ, 649, 14
Dijkstra M., Lidz A., Wyithe J. S. B., 2007, MNRAS, 377, 1175
Dijkstra M., Mesinger A., Wyithe J. S. B., 2011, MNRAS, 414, 2139
Draine B. T., 2003, ApJ, 598,
Erb D. K., Steidel C. C., Shapley A. E., Pettini M., Reddy N. A., Adelberger K. L., 2006, ApJ, 647, 128
Fardal M. A., Katz N., Weinberg D. H., Davé R., Hernquist L., 2001, ApJ, 562, 605
Faucher-Giguère C.-A., Lidz A., Hernquist L., Zaldarriaga M., 2008, ApJ, 688, 85
Faucher-Giguère C.-A., Kereš D., Dijkstra M., Hernquist L., Zaldarriaga M., 2010, ApJ, 725, 633
Field G. B., 1959, ApJ, 129, 551
Finkelstein S. L., Rhoads J. E., Malhotra S., Grogin N., 2009, ApJ, 691, 465
Finkelstein S. L. et al., 2011, ApJ, 729, 140
Forero-Romero J. E., Yepes G., Gottlöber S., Knollmann S. R., Cuesta A. J., Prada F., 2011, MNRAS, 415, 3666
Fujita A., Martin C. L., Mac Low M.-M., New K. C. B., Weaver R., 2009, ApJ, 698, 693
Fumagalli M., Prochaska J. X., Kasen D., Dekel A., Ceverino D., Primack J. R., 2011, MNRAS, 418, 1796
Furlanetto S. R., Schaye J., Springel V., Hernquist L., 2005, ApJ, 622, 7
Fynbo J. U., Møller P., Warren S. J., 1999, MNRAS, 305, 849
Geach J. E. et al., 2005, MNRAS, 363, 1398
Geach J. E., Smail I., Chapman S. C., Alexander D. M., Blain A. W., Stott J. P., Ivison R. J., 2007, ApJ, 655, L9
Genel S. et al., 2012, ApJ, 745, 11
Goerdt T., Dekel A., Sternberg A., Ceverino D., Teyssier R., Primack J. R., 2010, MNRAS, 407, 613
Haiman Z., Spaans M., 1999, ApJ, 518, 138
Haiman Z., Spaans M., Quataert E., 2000, ApJ, 537, L5
Hansen M., Oh S. P., 2006, MNRAS, 367, 979
Harrington J. P., 1973, MNRAS, 162, 43
Hayashino T. et al., 2004, AJ, 128, 2073
Hayes M. et al., 2010, Nat, 464, 562
Hayes M., Scarlata C., Siana B., 2011a, Nat, 476, 304
Hayes M., Schaerer D., Östlin G., Mas-Hesse J. M., Atek H., Kunth D., 2011b, ApJ, 730, 8
Hill G. J., Gebhardt K., Komatsu E., MacQueen P. J., 2004, in AIP Conf. Proc. Vol. 743, The New Cosmology: Conference on Strings and Cosmology. Am. Inst. Phys., New York, p. 224
Iliev I. T., Shapiro P. R., McDonald P., Mellema G., Pen U.-L., 2008, MNRAS, 391, 63
Jeeson-Daniel A., Ciardi B., Maio U., Pierleoni M., Dijkstra M., Maselli A., 2012, MNRAS, submitted (arXiv:1204.2554)
Joung M. R., Bryan G. L., Putman M. E., 2012, ApJ, 745, 148
Kennicutt R. C., Jr, 1998, ARA&A, 36, 189
Klein R. I., McKee C. F., Colella P., 1994, ApJ, 420, 213

Kollmeier J. A., Zheng Z., Davé R., Gould A., Katz N., Miranda-Escudé J., Weinberg D. H., 2010, ApJ, 708, 1048
Komatsu E. et al., 2009, ApJS, 180, 330
Kornei K. A., Shapley A. E., Erb D. K., Steidel C. C., Reddy N. A., Pettini M., Bogosavljevic M., 2010, ApJ, 711, 693
Kulas K. R., Shapley A. E., Kollmeir J. A., Zheng Z., Steidel C. C., Hairline K. N., 2012, ApJ, 745, 33
Latif M. A., Schleicher D. R. G., Spaans M., Zaroubi S., 2011, A&A, 532, A66
Laursen P., Sommer-Larsen J., 2007, ApJ, 657, L69
Laursen P., Sommer-Larsen J., Andersen A. C., 2009, ApJ, 704, 1640
Laursen P., Sommer-Larsen J., Razoumov A. O., 2011, ApJ, 728, 52
Law D. R., Steidel C. C., Shapley A. E., Nagy S. R., Reddy N. A., Erb D. K., 2012, ApJ, 745, 85
Lee J.-S., 1974, ApJ, 192, 465
McLinden E. M. et al., 2011, ApJ, 730, 136
Martin C. L., 1999, ApJ, 513, 156
Martin C. L., 2005, ApJ, 621, 227
Martin C. L., Bouché N., 2009, ApJ, 703, 1394
Matsuda Y. et al., 2004, AJ, 128, 569
Matsuda Y., Iono D., Ohta K., Yamada T., Kawabe R., Hayashino T., Peck A. B., Petitpas G. R., 2007, ApJ, 667, 667
Matsuda Y. et al., 2012, MNRAS, in press (arXiv:1204.4934)
Mori M., Umemura M., Ferrara A., 2004, ApJ, 613, L97
Murray N., Quataert E., Thompson T. A., 2005, ApJ, 618, 569
Nagamine K., Choi J.-H., Yajima H., 2010, ApJ, 725, L219
Neufeld D. A., 1990, ApJ, 350, 216
Neufeld D. A., 1991, ApJ, 370, L85
Nilsson K. K., Møller P., 2009, A&A, 508, L21
Nilsson K. K., Fynbo J. P. U., Møller P., Sommer-Larsen J., Ledoux C., 2006, A&A, 452, L23
Oppenheimer B. D., Davé R., 2006, MNRAS, 373, 1265
Oppenheimer B. D., Davé R., 2008, MNRAS, 387, 577
Prescott M. K. M., Smith P. S., Schmidt G. D., Dey A., 2011, ApJ, 730, L25
Prescott M. K. M. et al., 2012, ApJ, 752, 86
Prochaska J. X., Kasen D., Rubin K., 2011, ApJ, 734, 24
Rakic O., Schaye J., Steidel C. C., Rudie G. C., 2012, ApJ, 751, 94
Rauch M. et al., 2008, ApJ, 681, 856
Rosdahl J., Blaizot J., 2012, MNRAS, in press (doi:10.1111/j.1365-2966.2012.20883.x)
Rubin K. H. R., Prochaska J. X., Ménard B., Murray N., Kasen D., Koo D. C., Phillips A. C., 2011, ApJ, 728, 55
Rudie G. C. et al., 2012, ApJ, 750, 67
Rybicki G. B., Lightman A. P., 1979, Radiative Processes in Astrophysics. Wiley Interscience, New York, p. 393
Rybicki G. B., Loeb A., 1999, ApJ, 520, L79
Saito T., Shimasaku K., Ohamuia S., Ouchi M., Akiyama M., Yoshida M., 2006, ApJ, 648, 54
Santos M. R., 2004, MNRAS, 349, 1137
Scarlata C. et al., 2009, ApJ, 704, L98
Schaerer D., 2003, A&A, 397, 527
Shapley A. E., Steidel C. C., Pettini M., Adelberger K. L., 2003, ApJ, 588, 65
Smith D. J. B., Jarvis M. J., 2007, MNRAS, 378, L49
Steidel C. C., Adelberger K. L., Shapley A. E., Pettini M., Dickinson M., Giavalisco M., 2000, ApJ, 532, 170
Steidel C. C., Erb D. K., Shapley A. E., Puttini M., Reddy N. A., Bogosavljevic M., Rudie G. C., Rakic O., 2010, ApJ, 717, 289
Steidel C. C. et al., 2011, ApJ, 736, 160
Strickland D. K., Heckman T. M., 2009, ApJ, 697, 2030
Tasitsiomi A., 2006, ApJ, 645, 792
van de Voort F., Schaye J., Altay G., Theuns T., 2012, MNRAS, 421, 2809
Verhamme A., Schaerer D., Maselli A., 2006, A&A, 460, 397
Verhamme A., Schaerer D., Atek H., Tapken C., 2008, A&A, 491, 89
Wyithe J. S. B., Dijkstra M., 2011, MNRAS, 415, 3929
Yajima H., Li Y., Zhu Q., Abel T., 2012a, MNRAS, in press (arXiv:1109.4891)
Yajima H., Li Y., Zhu Q., Abel T., Gronwall C., Ciardullo R., 2012b, ApJ in press (arXiv:1112.1031)
Yamada T., Matsuda Y., Konsai K., Hayashino T., Morimoto N., Umemura M., 2012, ApJ, in press (arXiv:1203.3633)
Yang Y., Zabludoff A., Jahnke K., Eisenstein D., Davé R., Shectman S. A., Kelson D. D., 2011, ApJ, 735, 87
Zheng Z., Miralda-Escudé J., 2002, ApJ, 578, 33
Zheng Z., Cen R., Trac H., Miralda-Escudé J., 2010, ApJ, 716, 574
Zheng Z., Cen R., Trac H., Miralda-Escudé J., 2011a, ApJ, 726, 38
Zheng Z., Cen R., Weinberg D., Trac H., Miralda-Escudé J., 2011b, ApJ, 739, 62

APPENDIX A: CODE DESCRIPTION AND TESTING

We describe modifications to the code of Dijkstra et al. (2006) in detail. We test various subroutines of the new code in a simple geometry in which six clumps of radius $R_c = 10\,\mathrm{kpc}$ lie on the coordinate axes at a distance $d = 50\,\mathrm{kpc}$ from the origin, i.e. the clumps lie at $(x = \pm d, 0, 0)$, $(0, y = \pm d, 0)$ and $(0, 0, z = \pm d)$, where $d = 50\,\mathrm{kpc}$ (see Fig. A1). We assign an outflow velocity v_c to the clumps

In Section A1 we consider cases in which the clumps are transparent (i.e. $\tau \ll 1$) to Lyα, and in Section A2 we consider cases in which the clumps are extremely opaque to Lyα photons. For all these tests we assume that the gas temperature of the gas in the clumps is $T_c = 10^4\,\mathrm{K}$.

A1 Central source and transparent clumps

For these tests, we insert all Lyα photons at the origin and at the line resonance, i.e. $x_{in} = 0.0$.

A1.1 Testing the interclump propagation scheme

The sky covering factor of a single clump for a central source is $f_c = \Omega_c/4\pi$, where $\Omega_c = \pi\theta_c^2$ in which $\theta_c = \arcsin(R_c/d)$. The

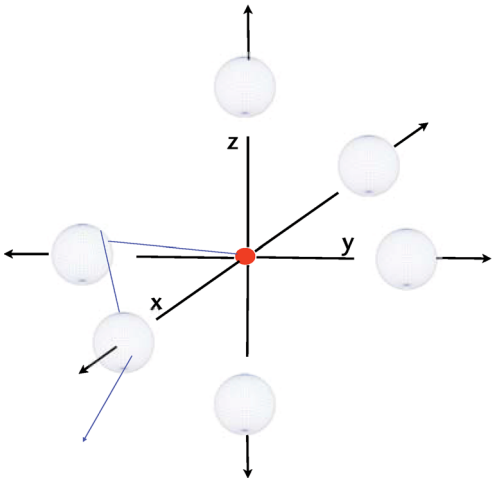

Figure A1. Clump geometry that we assumed in our test calculations. Six clumps of radius R_c lie on the coordinate axes at a distance $d = 50\,\mathrm{kpc}$ from the origin, which contains the source of Lyα photons. When the clumps are optically thin to Lyα photons, we can analytically compute the fraction of photons that scatter in N clumps as a function of N (see Section A1). When the clumps are opaque to Lyα photons (see Section A2), we can analytically compute the emerging spectrum.

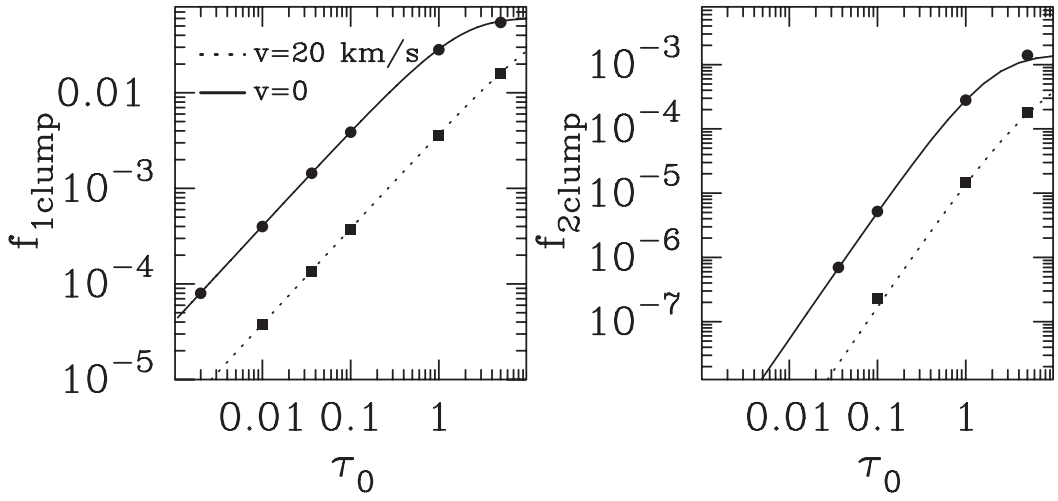

Figure A2. Comparison between analytic and Monte Carlo calculations of the fraction of photons that scatter in one clump (left-hand panel) and in two *distinct* clumps (right-hand panel) as a function of the line centre optical depth of an individual clump, τ_0, for $v_c = 0$ (solid lines) and $v_c = 20\,\mathrm{km\,s^{-1}}$ (dotted lines). The agreement is excellent, and shows that interclump and intraclump propagations – as well as frequency redistribution by moving clumps – are captured well by the Monte Carlo code.

fraction of photons that scatter in only one clump[15] is $f_{1\mathrm{clump}} = 6 \times f_c \times \langle 1 - \exp[-\tau(x_{\mathrm{in}})]\rangle$. Here $\langle 1 - \exp[-\tau(x_{\mathrm{in}})]\rangle$ is given by

$$\langle 1 - \exp[-\tau(x_{\mathrm{in}})]\rangle = \frac{2\pi}{\pi R^2}\int_0^R y\,\mathrm{d}y\left(1 - \exp\left[-\tau_0 \times \sqrt{\frac{R^2-y^2}{R^2}}\phi(x'[y])\right]\right). \quad \text{(A1)}$$

Here y denotes the impact parameter from the centre of the clump to where the photon strikes, τ_0 denotes the line centre optical depth through the centre of the clump and $\phi(x'[y])$ denotes the Voigt profile evaluated at $x' = x_{\mathrm{in}} - \frac{v_c}{v_{\mathrm{th}}}\cos\theta$, where θ denotes the angle between the photon's wavevector $\boldsymbol{k}$ and the outflow velocity vector $\boldsymbol{v}$, and we have $\cos\theta = \sqrt{1-\sin^2\theta} = \sqrt{1-(y/d)^2}$.

For example, for stationary clumps, the y-dependence of the term $\phi(x'[y])$ vanishes and the integral can be evaluated analytically when $\tau_0 \ll 1$, resulting in $f_{1\mathrm{clump}} \approx 0.0405\tau_0\phi(x)$. The left-hand panel of Fig. A2 compares analytically computed values of $f_{1\mathrm{clump}}$ for $v_c = 0$ (solid line) and $v_c = 20\,\mathrm{km\,s^{-1}}$ (dotted lines) as a function of τ_0, with those obtained from the Monte Carlo code. The agreement is excellent, and shows that interclump and intraclump propagations are captured well by the Monte Carlo code.

In the optically thin limit, we can also estimate the fraction of photons that scatter in two different clumps. An accurate estimate for this probability is given by

$$f_{2\mathrm{clump}} = f_{1\mathrm{clump}} \times \sum_{i\neq j}^{N_{\mathrm{clump}}} \frac{\Omega_{c,i}}{4\pi} P(\mu_i) \times \int_{-\infty}^{\infty} \mathrm{d}x'\,[\langle 1 - \exp -\tau_i(x')\rangle] R(x'|x[x_{\mathrm{in}}], \mu_i). \quad \text{(A2)}$$

This equation gives the probability that a photon scatters in a second clump, denoted with number 'i', *after having scattered in the first clump*, denoted with 'j'. The probability that the photon scatters in a second clump is a product of the probabilities that the photon scatters into a sightline that intersects clump 'i' and that it then scatters in that clump. This latter probability depends on the frequency of the photon after the first scattering event, and we integrate over all possible photon frequencies weighted by probability distribution function (PDF) of this frequency. A more detailed quantitative explanation follows below.

First, the probability that the photon scatters into a sightline that intersects clump 'i' is given by $\approx \frac{\Omega_{c,i}}{4\pi} P(\mu_i)$. In our test case, a photon has to scatter either by $\mu \approx -1$ for scattering in the clump on the same coordinate axis ($i = 5$) or $\mu \approx -1/\sqrt{2}$ for scattering in clumps on one of the other coordinate axes (i = 1–4). These probabilities are approximations – but accurate ones – because in reality the photons scatter into a (narrow) range of μ, which in detail depends on where exactly the first scattering event occurred. To capture this effect properly, we would have to average over μ weighted by the proper PDF for μ. However, since this range of μ only extends over $\Delta\mu \approx 0.2$, and because both $P(\mu)$ and $R(x'|x[x_{\mathrm{in}}], \mu_i)$ change very little over this range, this more detailed and tedious procedure barely changes our final results.

Secondly, the expression for the probability that a photon scatters in the second clump is given by $\langle 1 - \exp - \tau_i(x')\rangle$, which is given by equation A1 for $i = 5$ (with $d = 100$ kpc), but for i = 1–4 we omit the y-dependence of x'. The geometry for scattering in clumps i = 1–4 does not allow for a simple mapping between impact parameter y and Doppler boost, and this last modification represents a reasonable approximation.

Finally, the PDF for the outgoing photon frequency x' depends on both the scattering direction *and* incoming photon frequency x_{in}. We derive an analytic solution for the frequency redistribution function, $R(x''|x, \mu)$, which denote the PDF for x'' given x. These frequencies are measured in the frame of the gas. In our test case, photons appear at frequency $x = x_{\mathrm{in}} - v_c/v_{\mathrm{th}}$ in the frame of the first clump. The outgoing photon frequency x' (measured in the lab frame) relates to x'' through a Lorentz transformation: $x' = x'' + \mu v_c/v_{\mathrm{th}}$. The expression for $R(x''|x, \mu)$ is derived in Appendix C.

The right-hand panel of Fig. A2 compares the analytically computed values of $f_{2\mathrm{clump}}$ as a function of τ_0 for $v_c = 0$ (solid line) and $v_c = 20\,\mathrm{km\,s^{-1}}$ (dotted lines) with those obtained from our Monte Carlo code. The agreement is again excellent. This further illustrates that interclump and intraclump propagations of photons

[15] Formally, we have to multiply this probability $f_{1\mathrm{scat}}$ by the probability that photons do *not* subsequently scatter in other clumps. As the clump sky covering factor is only ∼6 per cent, this introduces a correction of at most a factor of ∼(1.0–0.06) = 0.94.

are described accurately. Furthermore, the (directional-dependent) frequency redistribution is also captured accurately.

A1.2 Testing the surface brightness and polarization subroutines

Dijkstra et al. (2006) focused on spherically symmetric gas distributions, which makes the calculation of the predicted surface brightness distribution straightforward. In 3D geometries ideally one has to compute the fraction of photons that escape from the medium, exactly in the direction of the telescope. Since the telescope is a cosmological distance removed from the location of the last scattering, and hence practically subtends an infinitesimally small fraction of the sky, this procedure is not possible in practice.

We follow a standard approach for computing surface brightness profiles, and compute the differential probability that a photon is scattered exactly towards the telescope, for each scattering event. This probability can be computed as follows. A photon scatters at some location $\boldsymbol{x}_{\rm scat} \equiv (x_{\rm s}, y_{\rm s}, z_{\rm s})$, by an atom whose velocity components are given by $\boldsymbol{v} \equiv (v_x, v_y, v_z)$, or by a dust grain whose thermal motion we neglect. We denote the photon's propagation, frequency and polarization before scattering with $\boldsymbol{k}_{\rm in}$, $x_{\rm in}$ and $\boldsymbol{e}_{\rm in}$. Now let us consider the $x^+ - y^+$ image. Photons that make up this image would have to be scattered into direction $\boldsymbol{k}_{\rm out} = (k_x, k_y, k_z) = (0, 0, 1)$.

The probability per steradian that a photon escapes into direction $\boldsymbol{k}_{\rm out}$ is

$$P = \exp[-\tau(x_{\rm out}, \boldsymbol{k}_{\rm out}, \boldsymbol{x}_{\rm out})] \times P(\boldsymbol{k}_{\rm in}, \boldsymbol{k}_{\rm out}, \boldsymbol{e}_{\rm in}|{\rm wing/res/dust}), \quad ({\rm A3})$$

where $x_{\rm out}$ is determined fully by $k_{\rm out}$, $x_{\rm in}$ and the velocity vector of the scattering atom, v (see equation C1), and where $P(\boldsymbol{k}_{\rm in}, \boldsymbol{k}_{\rm out}, \boldsymbol{e}_{\rm in}|{\rm wing/res/dust})$ denotes the phase function, which depends on whether the photon scatters in the line resonance, in the wings of the line or off a dust grain. For wing scattering the phase function depends on $\boldsymbol{e}_{\rm in}$ as $P(\boldsymbol{k}_{\rm out}, \boldsymbol{e}_{\rm in}|{\rm wing}) = \frac{3}{2}[1 - (\boldsymbol{k}_{\rm out} \cdot \boldsymbol{e}_{\rm in})^2]$ (Rybicki & Loeb 1999; Dijkstra & Loeb 2008a).

The total flux that the photon then contributes to the relevant pixel on the image – in this case at $(x_{\rm s}, y_{\rm s})$ – is given[16] by $S = \frac{\mathcal{L}}{4\pi d_{\rm L}^2(z)} \times P$, where $\mathcal{L} = L_{\rm tot}/N_\gamma$. Here, $L_{\rm tot}$ denotes the total Lyα luminosity of the source and N_γ denotes the total number of photons used in the Monte Carlo run (also see Tasitsiomi 2006; Laursen & Sommer-Larsen 2007).

Following Rybicki & Loeb (1999) the linear polarization $\mathcal{P}$ at a given location is determined by the *polarized* fluxes S_l and S_r as

$$\mathcal{P} \equiv \frac{S_r - S_{\rm l}}{S_r + S_l}. \quad ({\rm A4})$$

The total contribution of the photon to these polarized fluxes is given by

$$S_r = S \times \left[g(\mu)(1 - \cos^2\chi) + \tfrac{1}{2}(1 - g(\mu)) \right],$$
$$S_l = S \times \left[g(\mu)\cos^2\chi + \tfrac{1}{2}(1 - g(\mu)) \right], \quad ({\rm A5})$$

when a Lyα photon is scattered by a hydrogen atom. In this expression, $g(\mu) = 1$ for wing scattering and $g(\mu) = \frac{1+\mu^2}{11/3+\mu^2}$ for resonant scattering (Rybicki & Loeb 1999; Dijkstra & Loeb 2008a). Furthermore, χ denotes the angle between the photon polarization vector *after scattering*, denoted with $\boldsymbol{e}_{\rm out}$, and the vector $\boldsymbol{x}_{\rm scat}$ projected on to the x–y plane (as in Rybicki & Loeb 1999; Dijkstra & Loeb 2008a). In the case of wing scattering, $\boldsymbol{e}_{\rm out}$ is obtained by finding the normalized projection of the old polarization vector $\boldsymbol{e}_{\rm in}$ on to the plane normal to $\boldsymbol{k}_{\rm out}$ (Rybicki & Loeb 1999). In the case of resonant scattering, we generate a random unit vector perpendicular to $\boldsymbol{k}_{\rm out}$. Equation (A4) shows for example that scattering by 90° (i.e. $\mu = 0$) results in $\mathcal{P} = 1.0$ for wing scattering and $\mathcal{P} = 3/11$ for resonant scattering. When a Lyα photon scatters off a dust grain, we simply set $S_l = S_r = S/2$.

Fig. A3 shows the six images that we created from six directions (along the $\pm\hat{x}$, $\hat{y}$ and $\hat{z}$ directions) for a test problem in which $\tau_0 = 0.1$ and $v_{\rm c} = 0$ (see above). Because of our adopted geometry, the six images look identical within the noise as a result of the finite number of photons in the Monte Carlo run. The lower-right panel shows the image after taking the average of all six. Fig. A4 shows a close-up of the uppermost clump. This figure demonstrates that our images contain no flux where there is not supposed to be any. Furthermore, the surface brightness profile of individual clumps is in good agreement with analytic estimates: the *inset* shows a slice through the surface brightness map at $x = 0$ and plots the surface brightness – normalized to the maximum surface brightness in the clump – as a function of y. The histogram shows the result obtained from our Monte Carlo code, while the red solid line shows our analytic estimate, which we compute as follows.

The total flux that we expect to detect is $S(y) \propto \int_{-l(y)}^{l(y)} {\rm d}s\ \tau(y, s) f(s, y)$. Here, $f(y, s) \propto (y^2 + s^2)^{-1}$ denotes the incoming flux at position (y, s), where s denotes the position along the line of sight. This flux intersects the line of sight at an angle that increases with s, and the probability that the photon is scattered scales as $\tau \propto \sqrt{y^2 + s^2}/y$. We can therefore write $S(y) \propto \frac{1}{y}\int_{-l(y)}^{l(y)} {\rm d}s\ (y^2 + s^2)^{-1/2}$. At a given y, we know we will exit from the clump at $\pm l(y) = [R^2 - (d - y)^2]^{1/2}$. The resulting $S(y)$ – normalized to its maximum – is overplotted as the red solid line. The agreement between our analytic and Monte Carlo calculations is excellent, which further confirms that our surface brightness algorithm is working well.

We also found that the linear polarization lies in the range $\mathcal{P} =$ 23–27 per cent when measured across the four clumps that are not at $(x, y) = (0, 0)$ in the averaged image. This is very close to the maximum linear polarization, $\mathcal{P}_{\rm max,res} = 3/11$, that is expected from resonantly scattered Lyα radiation. The polarization of radiation coming from the central clumps is consistent with 0 in the centre and rises to $\mathcal{P} \sim 1$ per cent on the edges, which is again consistent with analytical expectations, which yield $\mathcal{P} = \frac{1-\mu^2}{11/3+\mu^2}$ (Dijkstra & Loeb 2008a). For scattering in the central clumps we have $\sin\theta \approx \tan\theta \approx y/d$, and the maximum polarization for the central clump is $\approx \frac{1}{25} \times \frac{3}{14} \approx 0.9$ per cent, which is in close agreement with our Monte Carlo calculations.

A2 Extremely opaque clumps with embedded Lyα sources

The previous sections showed that our code works well in the optically thin regime. These tests were important as they demonstrate the accuracy of our code with respect to resonant scattering, interclump and intraclump propagations, the surface brightness and polarization algorithms. In this section we briefly describe one test of scattering in an extremely opaque medium. This tests scattering in the wings of the line in greater detail.

[16] The standard factor of 4π is sometimes missing from the denominator in the literature (e.g. in Tasitsiomi 2006; Laursen et al. 2009), because of the normalization of the phase functions. Our phase functions are normalized as $\int {\rm d}\Omega P(\boldsymbol{k}_{\rm in}, \boldsymbol{k}_{\rm out}, \boldsymbol{e}_{\rm in}) \equiv 4\pi$.

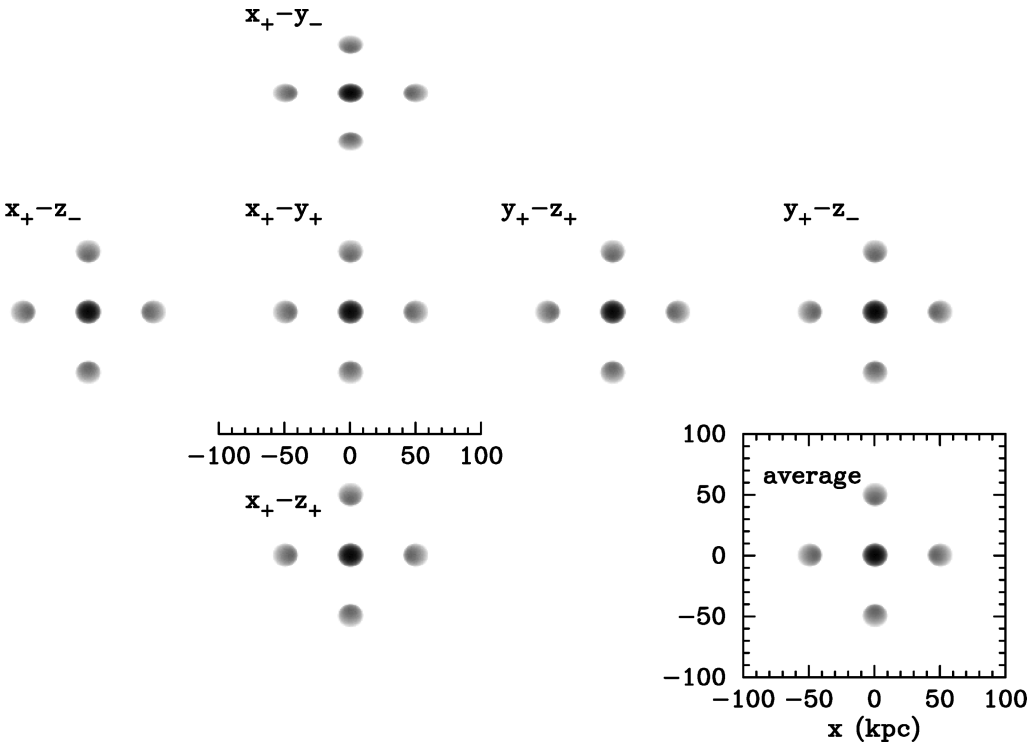

Figure A3. The surface brightness profiles for the scattered radiation are shown for all six viewing directions for a case in which $\tau_0 = 0.1$. The lower-right panel shows the average surface brightness profile. The central clump is approximately twice as bright as this contains emission that scattered from two clumps. This plot illustrates nicely that all scattered radiation is confined to regions associated with clumps. A more detailed view of a the surface brightness profile of a single clump in the averaged image is shown in Fig. A4

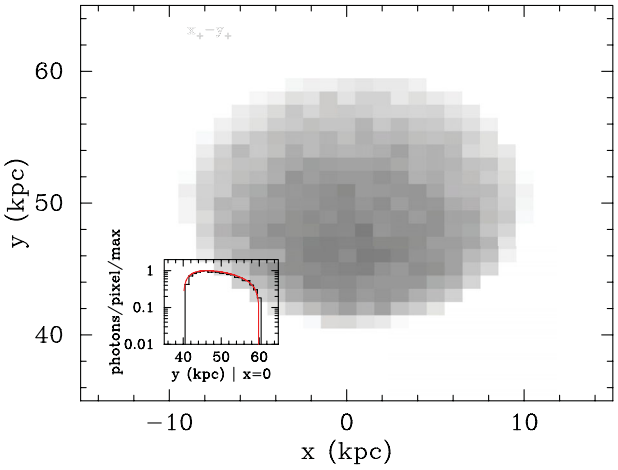

Figure A4. A more detailed view of the surface brightness distribution in the uppermost clump in the *averaged* image (shown previously in Fig. A3) is shown. The inset shows a slice through this distribution along the axis $x = 0$. The black histogram shows the normalized (to the maximum) surface brightness as a function of position y, which matches our analytic solution (red solid line) very well. This demonstrates that our surface brightness algorithm works well.

We insert photons at line centre in the centres of all clumps. The line centre optical depth through the clumps is enhanced to $\tau_0 = 10^7$. The spectrum of photons emerging from individual clumps is known analytically (Harrington 1973; Neufeld 1990; Dijkstra et al. 2006) and is given by

$$J_{\rm sph}(x) = \frac{\pi}{a_{\rm v}\tau_0\sqrt{24}} \frac{x^2}{1+\cosh\left[\sqrt{\frac{2\pi^4}{27}}\frac{|x|^3}{a_{\rm v}\tau_0}\right]}. \quad \text{(A6)}$$

This frequency x is measured in the frame of the clump. When a clump is outflowing, the proper Doppler boost should be applied. Under the – reasonable – assumption that a negligible fraction of the photons scatters in a second clump, the total spectrum of photons emerging from the six outflowing clumps can be given by

$$J(x) = \frac{1}{2\Delta x}\int_{x-\Delta x}^{x+\Delta x} {\rm d}x'\, J_{\rm sph}(x'), \quad \text{(A7)}$$

where $\Delta x = v_{\rm c}/v_{\rm th}$. The red solid line in Fig. A5 shows equation (A7) for $\tau_0 = 10^7$ and $v_{\rm c} = 100\,{\rm km\,s^{-1}}$, while the histogram shows the spectrum of photons that escape from out Monte Carlo simulation. This plot illustrates that our code treats scattering in the wing accurately. Further tests of our code regarding scattering in extremely opaque media were presented in Dijkstra et al. (2006) and Dijkstra & Loeb (2008a).

A3 Dust scattering and absorption

Analytic expressions for the fraction of photons that escape from uniform slabs (infinite plane parallel media) have been derived by Harrington (1973) and Neufeld (1990). Neufeld (1990) has provided an approximate expression for the escape fraction of Lyα photons for the case in which photons are emitted at line centre in the mid-plane of an 'extremely opaque' slab, where 'extremely opaque'

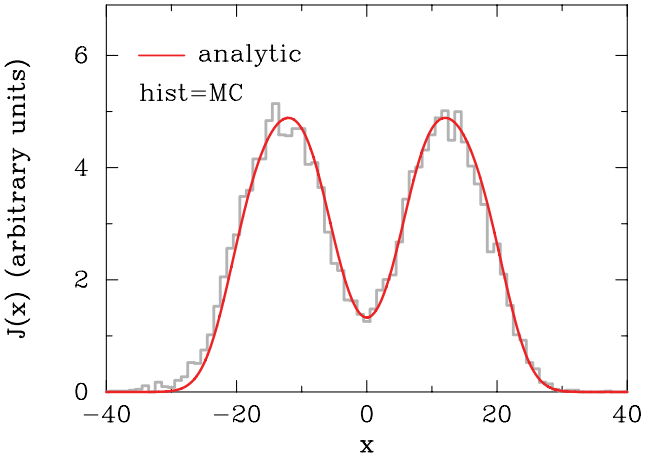

Figure A5. Spectrum of photons emerging from the six outflowing, optically thick clumps. Photons were emitted in the centres of all clumps. The red solid line shows the analytic solution (equation A7), while the histogram shows the solution that we obtain from our Monte Carlo simulation. This plot illustrates that our code treats scattering in the wing accurately.

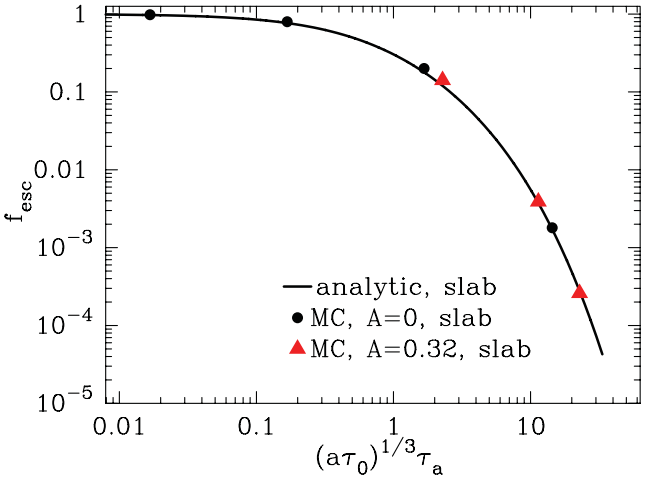

Figure A6. The escape fraction, $f_{\rm esc}$, of Lyα photons from a uniform slab as a function of dust *absorption* opacity, $\tau_{\rm a} \equiv (1-A)\tau_{\rm d}$, from the mid-plane to the edge of the slab. Here, $\tau_{\rm d}$ denotes the *total* dust opacity and A denotes the assumed albedo of the dust grains. The solid line shows the analytic solution of Neufeld (1990). The black filled circles (red filled triangles) denote the escape fraction obtained from our Monte Carlo code assuming $A = 0$ ($A = 0.32$). Destruction of Lyα photons is captured accurately in both cases of zero and non-zero albedo.

quantitatively means $a_{\rm v}\tau_0 \geq 10^3$. This expression[17] is

$$f_{\rm esc} = \left[\cosh\left(3.46(a_{\rm v}\tau_0)^{1/3}(1-A)\tau_{\rm d}\right)^{1/2}\right]^{-1}, \quad \text{(A8)}$$

where $\tau_{\rm d}$ is the *total* (absorption + scattering) optical depth in dust from the mid-plane to the edge of the slab and where A denotes the albedo. Fig. A6 shows that the escape fraction that we derive from our Monte Carlo code agrees very well with this analytic result for zero and non-zero dust albedos (as was also found by other authors, e.g. Laursen & Sommer-Larsen 2007; Forero-Romero et al. 2011; Yajima et al. 2012a).

[17] The numerical factor given in Neufeld (1990) also applies to our calculations, despite the different definition of τ_0. This is because the original approximate form derived by Neufeld (1990) is given by $f_{\rm esc} = 1/\cosh(Y_0^{1/2})$, where $Y_0 = [3\beta\phi(x_{\rm s})]^{1/2}\tau_0$. Here, $\beta \equiv (1-A)\tau_{\rm d}/\tau_0$ and $x_{\rm s} \equiv 0.525(a\tau_0)^{1/3}$. If we properly rescale $\tau_{0,\rm neufeld} \rightarrow \sqrt{\pi}\tau_{0,\rm us}$ and $\phi(x)_{\rm neufeld} \rightarrow \phi(x)_{\rm us}/\sqrt{\pi}$, then we get back the original equation.

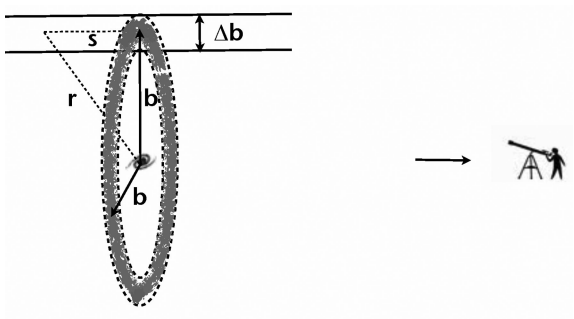

Figure B1. This figure depicts our adopted geometry and coordinates for the analytic calculation of the surface brightness profile of the scattered radiation.

APPENDIX B: DERIVATION OF ANALYTIC EXPRESSIONS FOR THE SURFACE BRIGHTNESS AND POLARIZATION PROFILES

The surface brightness (per unit area) of scattered radiation at impact parameter $b \pm \Delta b/2$ is given by

$$S(b) = \frac{1}{2\pi b\Delta b}\int_{-\infty}^{\infty} {\rm d}s\; 2\pi b \int_{-\infty}^{\infty} {\rm d}x \times f_{\rm esc}(x'', b, s) s_{\rm in}(s, b, x) p_{\rm scat}(s, b, x)\Delta b. \quad \text{(B1)}$$

The factor $2\pi b\ {\rm d}s\ s_{\rm in}(s, b, x)$ in the first line denotes the total flux incident on a ring of radius b at frequency x at line of sight coordinate s (see Fig. B1). The probability $p_{\rm scat}(s, b, x)\Delta b$ denotes the fraction of this flux that is scattered towards the observer. The probability $p_{\rm scat}(b, s, x)\Delta b = f_{\rm c}(r)\Delta b(r/b) \times (1 - \exp[-\tau_{\rm clump}(x', s, b)])$, where the first term denotes the probability that the photon hits a clump over the path of length $\Delta r = \Delta b(r/b)$, and the second term denotes the probability that the photon gets scattered by this particular clump. The incoming flux at location (b, s) and frequency x, as well as the expression for $\exp[-\tau_{\rm clump}(x', s, b)]$, is given in the main paper. The term $f_{\rm esc}(x'', b, s)$ denotes the fraction of the photons scattered at location (b, s) and frequency x, which are observed. Finally, in the main paper we expressed impact parameter in proper kpc, and we added a factor (kpc/asec)^2 to convert the surface brightness profile into the proper units of erg s^{-1} cm^{-2} arcsec^{-2}.

Equation (B4) is relevant for the total observed flux. We can derive the expressions for *polarized* fluxes $S_l(b)$ and $S_r(b)$ from the scattering matrix that describes scattering in the wing of the line, which is given by (Dijkstra & Loeb 2008a, and references therein)

$$R = \frac{3}{2}\begin{pmatrix} \mu^2 & 0 \\ 0 & 1 \end{pmatrix}, \quad \text{(B2)}$$

where the scattering matrix is defined as

$$\begin{pmatrix} I_l' \\ I_r' \end{pmatrix} = R \begin{pmatrix} I_l \\ I_r \end{pmatrix}. \quad \text{(B3)}$$

Here, I_l' and I_r' denote the components of the scattered intensity parallel and perpendicular to the plane of scattering, respectively. The incoming flux is coming directly from the source and is therefore likely unpolarized, in which case we have $I_l = I_r = \frac{1}{2}I$. We can

therefore write

$$\left.\begin{matrix} S_l(b) \\ S_r(b) \end{matrix}\right\} = \frac{3}{4} \times \frac{1}{2\pi b \Delta b} \int_{-\infty}^{\infty} \mathrm{d}s\, 2\pi b \int_{-\infty}^{\infty} \mathrm{d}x \times f_{\rm esc}(x'', b, s) s_{\rm in}(s, b, x) p_{\rm scat}(s, b, x) \Delta b \times \left\{ \begin{matrix} \mu^2 \\ 1 \end{matrix} \right. . \quad \text{(B4)}$$

APPENDIX C: DIRECTIONAL-DEPENDENT REDISTRIBUTION

The frequency redistribution function, often denoted with $R(x_{\rm out}|x_{\rm in})$, denotes the probability density function for the photon frequency $x_{\rm out}$ after scattering, given it had a frequency $x_{\rm in}$ prior to scattering. This function is an important quantity in the Lyα radiative transfer process, and analytic expressions have been known for decades (see e.g. Lee 1974, and references therein). The frequency redistribution function averages over all possible scattering angels, μ. However, the redistribution function varies strongly with μ: this is most evident when considering the case $\mu = 1$. Here, energy conservation implies that the photon frequency before and after scattering must be identical, and hence $R(x_{\rm out}|x_{\rm in}, \mu = 1) \neq R(x_{\rm out}|x_{\rm in})$. In this section we present a complete derivation of $R(x_{\rm out}|x_{\rm in}, \mu)$.

The photon frequencies before and after scattering are related[18] through the angle at which the photon is scattered, and the total 3D velocity of the hydrogen atom that scatters the photon as (e.g. Dijkstra et al. 2006)

$$x_{\rm out} = x_{\rm in} - \frac{\boldsymbol{v} \cdot \boldsymbol{k}_{\rm in}}{v_{\rm th}} + \frac{\boldsymbol{v} \cdot \boldsymbol{k}_{\rm out}}{v_{\rm th}} + g(\mu - 1) + \mathcal{O}\left(v_{\rm th}^2/c^2\right), \quad \text{(C1)}$$

where $g = h\Delta\nu_\alpha/(2k_{\rm B}T_{\rm c}) = 2.6 \times 10^{-4}(T_{\rm c}/10^4\,{\rm K})^{-1/2}$ is the fractional amount of energy that is transferred per scattering event (Field 1959). Throughout this calculation we safely ignore recoil (Adams 1971).

For simplicity, but without loss of generality, we can define a coordinate system such that $\boldsymbol{k}_{\rm in} = (1, 0, 0)$ and $\boldsymbol{k}_{\rm out} = (\mu, \sqrt{1-\mu^2}, 0)$, i.e. the photon wavevectors lie entirely in the x–y plane. Following Ahn, Lee & Lee (2000) we decompose the atom's velocity into components parallel ($v_{||}$) and orthogonal (v_y and v_z) to $\boldsymbol{k}_{\rm in}$, and we have $\boldsymbol{v} = (v_{||}, v_y, v_z)$. Equation (C1) can then be recast as

$$\begin{aligned} x_{\rm out} &= x_{\rm in} - \frac{v_{||}}{v_{\rm th}} + \frac{v_{||}\mu}{v_{\rm th}} + \frac{v_y\sqrt{1-\mu^2}}{v_{\rm th}} \\ &\equiv x_{\rm in} - u + u\mu + w\sqrt{1-\mu^2}, \end{aligned} \quad \text{(C2)}$$

where we have introduced the dimensionless velocity parameters $u = v_{||}/v_{\rm th}$ and $w = v_{\rm y}/v_{\rm th}$. Note that the value of v_z is irrelevant in this equation.

[18] This assumes coherence in the frame of the atom, which is relevant at the densities and temperatures of interest (see e.g. Dijkstra et al. 2006, for a more detailed discussion).

The velocities u and w are unrelated, and the most general way of writing the directional redistribution function is

$$R(x_{\rm out}|\mu, x_{\rm in}) = \mathcal{N} \int_{-\infty}^{\infty} \mathrm{d}u \int_{-\infty}^{\infty} \mathrm{d}w \times R(x_{\rm out}|\mu, x_{\rm in}, u, w) P(u|\mu, x_{\rm in}) P(w|\mu, x_{\rm in}), \quad \text{(C3)}$$

where $\mathcal{N}$ denotes the normalization constant. The integral over w can be eliminated by utilizing equation (C2), i.e. we replace $R(x_{\rm out}|\mu, x_{\rm in}, u, w) = \delta_{\rm D}(f[w_u]) = \delta_{\rm D}(w - w_u)/\frac{\mathrm{d}f}{\mathrm{d}w}$, in which $f[w_u] = x_{\rm out} - x_{\rm in} + u - u\mu - w_u\sqrt{1-\mu^2}$. We find

$$R(x_{\rm out}|\mu, x_{\rm in}) = \mathcal{N} \int_{-\infty}^{\infty} \mathrm{d}u\, P(u|\mu, x_{\rm in}) P(w_u|\mu, x_{\rm in}), \quad \text{(C4)}$$

where the factor $1/\frac{\mathrm{d}f}{\mathrm{d}w} = 1/\sqrt{1-\mu^2}$ is absorbed by the normalization constant $\mathcal{N}$.

The conditional absorption probabilities for both w and u cannot depend on the subsequent emission direction, and therefore $P(u|\mu, x_{\rm in}) = P(u|x_{\rm in})$ and $P(w_u|\mu, x_{\rm in}) = P(w_u|x_{\rm in})$. Furthermore, the conditional PDF for w does not depend on $x_{\rm in}$ either. This is because w denotes the normalized velocity of the scattering atom in a direction perpendicular to $\boldsymbol{k}_{\rm in}$, and the frequency that the atoms 'see' does not depend on w. The absorption probability can therefore not depend on w, and $P(w_u|x_{\rm in}) = P(w_u) = \sqrt{\frac{m_{\rm p}}{2\pi k_{\rm B}T}}\exp(-w_u^2)$, where we assumed a Maxwell–Boltzmann distribution for the atoms' velocities.

The expression for $P(u|x_{\rm in})$ can be obtained from Bayes theorem (see e.g. Lee 1974), which states that $P(u|x_{\rm in}) = P(u, x_{\rm in})/P(x_{\rm in}) = P(x_{\rm in}|u)P(u)/P(x_{\rm in})$, in which $P(x_{\rm in}|u)$ denotes the absorption probability for a single atom that has a speed u, and $P(x_{\rm in}) \propto \sigma(x_{\rm in})$. Therefore, $P(u|x_{\rm in}) \propto P(x_{\rm in}|u)P(u)/\sigma(x_{\rm in})$, where $P(x_{\rm in}|u) = \frac{3\lambda_\alpha^2}{8\pi}\frac{A_\alpha^2}{[\omega_\alpha(x_{\rm in}-u)v_{\rm th}/c]^2 + A_\alpha^2/4}$ (e.g. Rybicki & Lightman 1979). If we substitute this into equation (C4) and absorb all factors that can be pulled out of the integral into the normalization constant $\mathcal{N}$, then we get

$$R(x_{\rm out}|\mu, x_{\rm in}) = \mathcal{N} \int_{-\infty}^{\infty} \mathrm{d}u \frac{\exp(-u^2)}{(x_{\rm in} - u)^2 + a_{\rm v}^2} \times \exp\left[-\left(\frac{\Delta x + u(\mu - 1)}{\sqrt{1-\mu^2}} \right)^2 \right], \quad \text{(C5)}$$

where we introduced $\Delta x \equiv x_{\rm in} - x_{\rm out}$. The normalization constant can be computed analytically, and we have

$$R(x_{\rm out}|\mu, x_{\rm in}) = \frac{a_{\rm v}}{\pi^{3/2}\phi(x_{\rm in})\sqrt{1-\mu^2}} \int_{-\infty}^{\infty} \mathrm{d}u \frac{\exp(-u^2)}{(x_{\rm in} - u)^2 + a_{\rm v}^2} \times \exp\left[-\left(\frac{\Delta x + u(\mu - 1)}{\sqrt{1-\mu^2}} \right)^2 \right] \quad \text{for } |\mu| < 1. \quad \text{(C6)}$$

For $\mu = 1$ we have $x_{\rm out} = x_{\rm in}$ (equation C2). For $\mu = -1$ we have $x_{\rm out} = x_{\rm in} - 2u$, and we have $R(x_{\rm out}|\mu = -1, x_{\rm in}) = \frac{1}{2}P(u_{\rm c}|x_{\rm in})$, in which $u_{\rm c} = (x_{\rm in} - x_{\rm out})/2$. We have verified that these analytic expressions are in excellent agreement with results obtained from Monte Carlo calculations.

This paper has been typeset from a TEX/LATEX file prepared by the author.